

Imaging Through Scattering

by

Guy Satat

B.Sc., Technion, Israel Institute of Technology (2013)

Submitted to the Program in Media Arts and Sciences,
School of Architecture and Planning,
in partial fulfillment of the requirements for the degree of

Master of Science in Media Arts and Sciences

at the

MASSACHUSETTS INSTITUTE OF TECHNOLOGY

June 2015

© Massachusetts Institute of Technology 2015. All rights reserved.

Author
Program in Media Arts and Sciences,
School of Architecture and Planning,
May 8, 2015

Certified by.....
Ramesh Raskar
Associate Professor
Thesis Supervisor

Accepted by.....
Pattie Maes
Academic Head
Program in Media Arts and Sciences

Imaging Through Scattering

by

Guy Satat

Submitted to the Program in Media Arts and Sciences,
School of Architecture and Planning,
on May 8, 2015, in partial fulfillment of the
requirements for the degree of
Master of Science in Media Arts and Sciences

Abstract

In this thesis we demonstrate novel methods to overcome optical scattering in order to resolve information about hidden scenes, in particular for biomedical applications. Imaging through scattering media has long been a challenge, as scattering corrupts scenes in a non-invertible way. The use of near-visible optical spectrum for biomedical purposes has many advantages, such as optical contrast, optical resolution and non-ionizing radiation. Particularly, it has important applications in biomedical imaging, such as sub-dermal imaging for diagnostics, screening and monitoring conditions.

We demonstrate methods to overcome and use scattering in order to recover scene parameters. In particular we demonstrate a method for locating and classifying fluorescent markers hidden behind turbid layers using ultrafast time-resolved measurements with a sparse-based optimization framework. This novel method has applications in remote sensing and *in-vivo* fluorescence lifetime imaging.

Another method is demonstrated to resolve blood flow speed within skin tissue. This method is based on a computational photography technique and coherent illumination. This method can be applied in diagnosis and monitoring of burns, wounds, prostheses and cosmetics. A particularly important application of this technology is analysis of diabetic ulcers, which is the main cause for non-traumatic amputations in India. The suggested prototype is suitable for assisting clinicians in assessing the wound healing process.

The methods developed in this thesis using ultrafast time-resolved measurements, sparsity-based optimization and computational photography can spur research and applications in biomedical imaging, skin conditions diagnosis and more general modalities of imaging through scattering media.

Thesis Supervisor: Ramesh Raskar
Title: Associate Professor

Imaging Through Scattering
by
Guy Satat

Thesis Advisor.....
Ramesh Raskar
Associate Professor of Media Arts and Sciences
MIT Program in Media Arts and Sciences

Thesis Reader
Edward Boyden
Associate Professor of Media Arts and Sciences
MIT Program in Media Arts and Sciences

Thesis Reader
Joseph A. Paradiso
Associate Professor of Media Arts and Sciences
MIT Program in Media Arts and Sciences

Acknowledgments

This work would not have been possible without the help of my family, mentors and colleagues.

I would like to thank my advisor Prof. Ramesh Raskar for his guidance and support throughout this journey. I would also like to thank my thesis readers, Prof. Ed Boyden and Prof. Joe Paradiso, for their insightful comments and suggestions.

I am thankful to my wife Talia, for her love, support and help with the editing process. I would also like to thank my parents, sister and grandparents, for their love and care, and for pushing me to pursue great challenges.

This work would not have been possible without the support of the Camera Culture members who took part in this research and helped me along the way, in particular Christopher Barsi, Dan Raviv and Barmak Heshmat.

This research was supported by the experimental setup provided by Prof. Mounqi Bawendi. Funding was provided by the MIT Tata Center.

Contents

| | | |
|----------|---|-----------|
| 1 | Introduction | 19 |
| 1.1 | Motivation | 19 |
| 1.1.1 | Fluorescence Lifetime Imaging in Scattering Media | 20 |
| 1.1.2 | Blood Flow Speed Measurement with Coherent Scattering | 20 |
| 1.2 | Novelty and Main Contributions | 21 |
| 2 | Background and Related Work | 23 |
| 2.1 | Scattering and Diffusion Theory | 23 |
| 2.2 | Photon Diffusion Equation | 25 |
| 2.3 | Coherent Scattering — Speckle | 26 |
| 2.4 | Methods to Image through Scattering | 27 |
| 2.5 | Imaging Blood Flow Speed with Laser Speckle Contrast Imaging (LSCI) | 32 |
| 3 | Fluorescence Lifetime Imaging in Scattering Media | 33 |
| 3.1 | Ultrafast Measurements Using a Streak Camera | 34 |
| 3.2 | Forward Model | 35 |
| 3.3 | Reconstruction Algorithm | 39 |
| 3.3.1 | Step 1: Geometry Reconstruction | 40 |
| 3.3.2 | Step 2: Lifetime Reconstruction | 42 |
| 3.3.3 | OMP Stopping Criteria | 42 |
| 3.3.4 | Algorithm Parameters | 43 |
| 3.4 | Experimental Demonstration | 44 |
| 3.4.1 | Optical Setup | 45 |

| | | |
|----------|--|-----------|
| 3.5 | Noise and Sensitivity Analysis | 48 |
| 3.6 | Accessible Volume | 49 |
| 3.7 | Comparison to Previous Methods | 52 |
| 3.8 | Discussion | 54 |
| 4 | Blood Flow Speed Measurement with Coherent Scattering | 55 |
| 4.1 | Theory of LSCI | 55 |
| 4.2 | Rejecting Subsurface Scattering for LSCI | 59 |
| 4.3 | Synthetic Results | 60 |
| 4.3.1 | Simulation Methods | 60 |
| 4.3.2 | Simulation Results | 62 |
| 4.4 | Experimental Results | 65 |
| 4.4.1 | Experimental Prototype | 65 |
| 4.4.2 | Experimental Results | 66 |
| 4.5 | Technical Discussion | 69 |
| 4.6 | Applications and Business Perspective | 69 |
| 5 | Conclusions | 73 |

List of Figures

| | | |
|-----|---|----|
| 2-1 | Figure from Vogel and Venugopalan 2003 [95]. Absorption and scattering in biological tissue. a) Absorption coefficient vs. optical wavelength in the range of $0.1 - 10\mu m$. b) Scattering coefficient (normalized by the absorption coefficient) vs. optical wavelength in the range of $400 - 1800nm$. Scattering outside of this range is not characterized since it is dominant by absorption. | 24 |
| 2-2 | Different events a photon can undergo during transport in complex media. | 25 |
| 2-3 | Speckle formation from a rough surface. | 27 |
| 3-1 | Sample fluorescence lifetime measurement with a streak camera. a) Set of 3 non-fluorescing patches hidden behind a diffuser. b) 2 fluorescing patches with decay times extending throughout the entire image (recorded without UV filter). The diffuser is fluorescent, noted by the decay of the calibration spot in the bottom left part of the images. Scale bars: 4.2 cm (horizontal), 200 ps (vertical). | 34 |
| 3-2 | Geometry of diffuser and patch | 35 |
| 3-3 | A simulated streak image for: a) a non-fluorescing patch, that is $\tau \rightarrow 0$, and b) a fluorescing patch with $\tau = 5ns$. Scale bar: 100ps (vertical) and 1cm (horizontal). | 38 |

| | | |
|------|--|----|
| 3-4 | Time-resolved fluorescence imaging with a pulse train. a) Incident pulse train, separated by period T . b) Measured output for a fluorescing marker with lifetimes $5ns$ and $32ns$. Dashed lines indicate the individual response for a single pulse. Solid lines indicate the measured signal. The orange box indicates detector time window. | 39 |
| 3-5 | Reconstruction algorithm flow. Raw measurements are filtered to produce streak hyperbolas; geometry is recovered via OMP; a lifetime dictionary is created; and another OMP step identifies lifetimes of the probes. | 40 |
| 3-6 | Dictionary construction flow. A patch is computationally moved in the interest volume to generate the corresponding L streak images which are vectorized in the dictionary columns. The column number corresponds to specific patch locations in the volume. | 42 |
| 3-7 | Residual error decrease rate versus number of patches considered in the OMP solution. The dashed lines represents the location in which the stopping criterion has reached. | 43 |
| 3-8 | Experimental geometry. a) Experimental setup. b) Scene under investigation. | 44 |
| 3-9 | Experimental measurements as input to the algorithm. Each column is a different configuration, and for each we show a) example of four measurements taken and b) the corresponding high-pass filtered images. Scale bars: $4.2cm$ (horizontal), $200ps$ (vertical). The four points correspond to measurements with illumination positions x12, x11, x9, x8 as shown by the labels in Fig. 3-11. | 45 |
| 3-10 | Reconstruction results. a) Reconstructed streak images using the recovered locations and lifetimes. b) Geometry recovered for each configuration. Green and yellow correspond to PI and QD patches, respectively. Patches with an X are the recovered locations; solid outlines indicate ground truth (measured by a Faro Gage Arm). | 46 |

| | | |
|------|--|----|
| 3-11 | Experimental setup. A 1.15 Watt Ti:Sapphire beam is frequency-doubled and is focused onto a diffuser via a pair of galvo mirrors (GM), which scan the beam across the diffuser to different incident positions (inset). Light is scattered by various objects and is recorded by a streak camera (field of view indicated by the dotted line). A fixed reference beam is used to correct intensity and timing noise. Inset: locations of incident laser positions for each streak image. | 47 |
| 3-12 | Patch size effect on PSNR. The red dots are experimental measurements (taken with fixed exposure and gain), and the blue curve is a forward model simulation prediction (to simulated measurements we add white Gaussian noise with variance that matches the measured variance). | 48 |
| 3-13 | Noise performance. a) Analysis of reconstruction error as function of patch side size and added noise. White Gaussian noise with increasing variance (x-axis) is added while increasing the patch's size (y-axis). The color represents the total algorithm reconstruction error in arbitrary units. Inset figure shows the algorithm sensitivity along the black dashed line (corresponding to patch size of $1.5cm$). b) Examples of different points on the inset graph which show input images with added noise and the reconstruction results. These images correspond to one of the twelve illumination points. | 50 |
| 3-14 | Visible volume. a) Top and b) side views of visible volume. The inner black curve shows the saturation bound, and the outer black curve shows the noise-limited bound. The purple area shows the geometry limitation imposed by diffusion/scattering angles (σ). The green rectangle in the middle of the diffuser is the line imaged by the camera (conventional FoV). c) Illumination gaps due to small scattering angles and widely-spaced illumination points. | 52 |

| | | |
|-----|--|----|
| 4-1 | Left: speckle formation from a rough static surface has high contrast. Right: Speckle formation from a rough dynamic surface produces low contrast images. | 57 |
| 4-2 | An example of mapping from speckle image to perfusion map using Eq. 4.9 and a spatial window. | 59 |
| 4-3 | Light rays are captured from both the surface and subsurface. The sensor measures the intensity of (D), which is a result of direct illumination (A) and global scattering (B) + (C). Many ray paths can contribute to global light. | 60 |
| 4-4 | Global light produces erroneous contrast maps for skin perfusion. Left: a single layer of dynamic scattering can be reconstructed easily. Right: a second layer compounds the contrast image, and the resulting speed map is incorrect. | 61 |
| 4-5 | Simulated scene with two scattering layers. The black characters indicate areas of high speed. Incident speckle illumination scatters to the first layer, then to the second. Both are recorded simultaneously for four different incident illumination patterns. | 61 |
| 4-6 | Synthetic results demonstrating benefits of global-direct separation for skin perfusion. (a) Scene ground truth: speed maps indicate areas of relative motion, and reflectance maps indicate the contrast measurement of each layer in the absence of the other. (b) Four measurements, illuminated by different speckle patterns. (c) Decomposition to direct component reflectance (top), the sum of measurements as a baseline (bottom). (d) Speed reconstruction based on the corresponding intensity maps. The reconstruction based on the direct component reproduces the speed map of the front layer, whereas the baseline result contains speed contributions from both layers. | 63 |

| | | |
|------|---|----|
| 4-7 | Simulation speed reconstruction error for a varying number of illumination sources and measurement noise. The baseline (left) and our suggested method (right) show the reconstruction error for various measurement noise (SNR) and illumination patterns. | 65 |
| 4-8 | Simulation speed reconstruction error for a varying number of illumination sources and internal layer depth z . The baseline (left) and our suggested method (right) show the reconstruction error for various measurement noise (SNR) and illumination patterns. | 66 |
| 4-9 | Experimental setup. Left: system block diagram. Right: picture of the imaging system used. | 67 |
| 4-10 | Experimental results of a healthy hand. a) The four measurements. Speckle images and corresponding speed maps for baseline (b), global component (c), and direct component (d). | 68 |
| 4-11 | Experimental results of a superficial burn. a) the four measurements, the burn is circled in red on the bottom picture. Speckle images and corresponding speed maps for baseline (b), global component (c), and direct component (d). | 68 |

List of Tables

| | | |
|-----|--|----|
| 3.1 | Reconstruction error. The numbers represent distances from the center of each ground truth patch in space to the center of the corresponding reconstructed patch (length units are millimeters). | 45 |
| 3.2 | Comparison between different methods: a. our method, b. FDOT approach [38], c. streak-based with simple optimization [63], d. streak-based with back propagation [94], e. SLM-based [49] and f. speckle correlation approach [46]. | 53 |

Chapter 1

Introduction

In the following section we describe the motivation and main contributions of our work.

1.1 Motivation

Imaging through scattering is a long lasting problem in optics, as scattering invalidates imaging conditions. Scattering appears in numerous cases such as astronomy, medical imaging, and imaging through fog, sandstorms and air turbulence.

Imaging is an important tool for health diagnostics, as can be appreciated from the number of Nobel prizes awarded for different imaging modalities (X-ray - 1901, CT - 1979 and MRI - 2003). While these methods all use the x-ray part of the spectrum, there are many advantages to using the visible and near-visible part of the spectrum:

- Non-ionizing radiation.
- Optical contrast — since molecules interact with the visible spectrum in many different ways, there is more to be learned about the tissue in this range (as a counter example, x-ray based methods have difficulties to distinguish between different types of soft-tissue).
- Resolution — using the optical range provides better resolution compared to ultrasound based methods.

In this thesis we demonstrate novel methods to overcome scattering, as well as how scattering can be of use in the context of biomedical imaging. Specifically we show how ultrafast time-resolved measurements combined with novel signal processing allow to reconstruct a scene hidden behind scattering media, and to classify fluorescing markers. Additionally we demonstrate a computational photography technique to measure blood flow speed in skin tissue using coherent scattering, and we discuss real-world applications of this technique.

1.1.1 Fluorescence Lifetime Imaging in Scattering Media

The use of fluorescing markers and measurement of their fluorescence lifetimes allow for significant advances in many imaging systems, in particular medical imaging systems. Fluorescing markers are already widely used as contrast agents and as a tool to improve imaging resolution [39, 56]. Other applications of fluorescing markers include study of turbulence [11, 15], high temperature reactions [61], remote sensing of vegetation [37] and covert tracking [101]. One of the important parameters of fluorescence is the lifetime which varies as a function of the environment; careful engineering of this interaction followed by fluorescence lifetime measurement can serve as an in-vivo probe [77]. Therefore, fluorescence lifetime imaging microscopy (FLIM) has become an important tool for biopsy analysis of thin layered tissue [52]. However, FLIM is limited to thin sliced tissues, which limits its applicability to in-vivo imaging.

1.1.2 Blood Flow Speed Measurement with Coherent Scattering

While scattering is usually an unwanted phenomenon, it can be useful if the scatterers are the target signal. One example of this is the imaging of blood cells with coherent illumination. The scattering from the cells results in an interference pattern on the detector plane known as speckle [28]. It has been previously shown that the speckle pattern encodes some of the scatterers' properties, specifically their movement [23]. This resulted in a set of methods to measure blood flow speed known as laser speckle

contrast imaging (LSCI) [9]. The main drawback of these methods is their qualitative results; many different attempts have been made in order to make it more quantitative (see section 2.5), and this research field is still very active.

1.2 Novelty and Main Contributions

This thesis makes important contributions to scattering analysis, specifically how to overcome and use scattering in order to resolve information about a hidden scene.

- a) **Using ultrafast time-resolved measurements to overcome scattering and resolve location and lifetime of fluorescing markers.** As mentioned above, fluorescence lifetime imaging provides an important tool for in-vivo probing. We demonstrate a novel method to recover location and lifetime of fluorescing markers hidden behind turbid layers [81]. This method is based on ultrafast measurements (performed with a streak camera) combined with an optimization framework. Our method allows advancements in many other applications such as non-invasive diagnosis, analysis, flowmetry and inspection.

- b) **Using scattering to increase field of view.** Diffusion can actually be used as a mean to converge (focus) light from areas outside the camera's field of view. Although this light does not directly provide information on its source (as it undergoes scattering), some of the source properties are encoded in the measurement. We show that a measurement using a streak camera, which is imaging just a single line in space, can result in a reconstruction of a complete three-dimensional volume behind a diffusive layer [81]. This concept opens the door to non-traditional imaging devices and lenses.

- c) **Using a combination of coherent scattering and computational photography to resolve blood flow speed.** The use of laser speckle contrast analysis for blood flow measurement, and skin perfusion analysis in particular, has been suggested in [9]. We demonstrate that augmenting this method with a

computational photography technique that rejects non-coherent scattering significantly improves the flow estimation results [80]. This new method makes the technique more robust and suitable for real-world applications, which include applications for prediction of wounds and burns recovery, and during plastic and reconstructive surgeries [86].

Business analysis and applications in India. We provide initial application and business analysis for this technique on skin conditions diagnosis.

Chapter 2

Background and Related Work

2.1 Scattering and Diffusion Theory

First, we introduce basic terminology in scattering theory with emphasis on biological tissue and visible to near-infrared (NIR) spectrum ($400 - 1350nm$). In this spectrum range most biological tissues are characterized by strong scattering and low absorption (see figure 2-1) [95]. Hence it is considered as the imaging window into biological samples.

Propagation of electromagnetic radiation in scattering media is characterized by different length scales which are defined by:

- Scattering mean free path, defined as the average distance between two consecutive scattering events. In tissue it is of the order of $0.1mm$ [99]. The scattering coefficient μ_s is defined as the inverse of the scattering mean free path.
- Mean absorption path, defined as the average distance a photon travels before it is absorbed in the medium. In tissue it can extend to $10 - 100mm$ [99]. The absorption coefficient μ_a is defined as the inverse of the mean absorption path.
- Mean free path (MFP), defined as the distance a photon travels before it is scattered or absorbed. The MFP is defined by its inverse — the transport coefficient μ_t , such that $\mu_t = \mu_a + \mu_s$. In tissue usually $\mu_s \gg \mu_a$ such that the mean free path is simply the scattering mean free path.

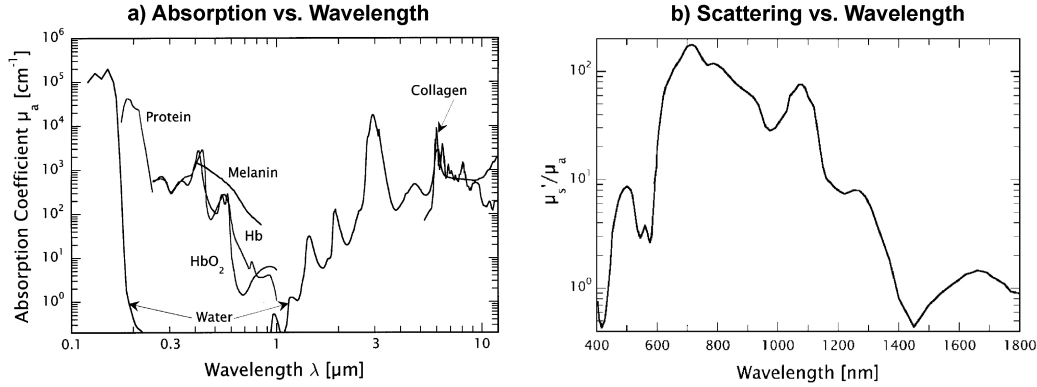


Figure 2-1: Figure from Vogel and Venugopalan 2003 [95]. Absorption and scattering in biological tissue. a) Absorption coefficient vs. optical wavelength in the range of $0.1 - 10\mu\text{m}$. b) Scattering coefficient (normalized by the absorption coefficient) vs. optical wavelength in the range of $400 - 1800\text{nm}$. Scattering outside of this range is not characterized since it is dominant by absorption.

- Transport mean free path (TMFP), defined as the distance a photon propagates while it undergoes several scattering events and is still correlated to the original direction. Similarly, it is defined by the inverse μ'_s such that $\mu'_s = \mu_s(1-g)$ where g is the anisotropy function which defines the degree of forward scattering, in tissue $g \sim 0.9$ [67].

When a photon interacts with a scattering medium it can undergo several events [6](see figure 2-2):

- Specular reflection — from the surface of the medium.
- Absorption — within the medium.
- Diffuse reflection — after going through one or more scattering events within the medium.
- Direct transmission — no interaction with the medium (ballistic photons).
- Diffuse transmission — transmission through the medium after going through one or more scattering events. These photons are usually divided into:
 - Snake photons, which undergo very little scatterings.
 - Diffused photons, which go through significant amount of scattering.

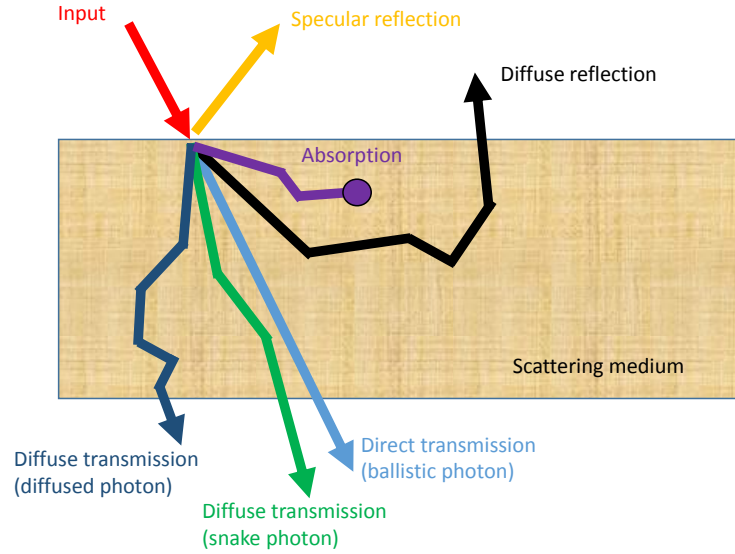


Figure 2-2: Different events a photon can undergo during transport in complex media.

2.2 Photon Diffusion Equation

It is common to write a conservation equation to describe the propagation of energy within a scattering medium. The equation is written for infinitesimal voxels and usually ignores interaction between the photons (i.e. interference). This is known as the Boltzmann transport equation [6]:

$$\frac{1}{\nu} \frac{\partial L(r, \Omega, t)}{\partial t} + \nabla \cdot L(r, \Omega, t) \Omega + \mu_t L(r, \Omega, t) = \mu_s \int_{4\pi} f(\Omega, \Omega') L(r, \Omega', t) d\Omega' + Q(r, \Omega, t) \quad (2.1)$$

where ν is the speed of light in the medium, $L(r, \Omega, t)$ is the radiance at position r with direction Ω at time t , $f(\Omega, \Omega')$ is the scattering phase function and $Q(r, \Omega, t)$ are sources. As in a standard conservation equation, the left hand side represents outgoing radiance, and the right hand side represents incoming radiance. We now discuss the physical meaning of each term from left to right: 1) The time derivative of the radiance, i.e. the net change of radiance in a small voxel at a given time point. 2) The radiance flux at direction Ω . 3) Accounts for absorption in the medium and scattering in the direction Ω . 4) Scattering from all directions to direction Ω ; this is

the balance to term no. 3. 5) Sources in the voxel.

The main problem with equation 2.1 is its complication. A common simplification to the Boltzmann transport equation is the photon diffusion equation which is a zero order approximation [17]. The diffusion equation is expressed with the photon fluence rate $\Phi(r, t)$ such that $\Phi(r, t) = \int L(r, \Omega, t) d\Omega$. This approximation is valid when the radiance is almost uniform with respect to the angle parameter. The photon diffusion equation is:

$$-\nabla \cdot D \nabla \Phi(r, t) + \nu \mu_a \Phi(r, t) + \frac{\partial \Phi(r, t)}{\partial t} = \nu S(r, t) \quad (2.2)$$

where $S(r, t) = \int Q(r, \Omega, t) d\Omega$ (i.e. a uniform source), and $D = \nu / 3\mu'_s$ is the diffusion coefficient [6] (sometime the diffusion coefficient contains an absorption term [20, 21]).

Diffusion-based models ignore interaction of photons with themselves, thus they are not suitable for coherent sources. The next section discusses the theory of coherent scattering.

2.3 Coherent Scattering — Speckle

Speckle is a result of coherent light scattered from a rough surface. This section will mainly discuss reflection but the theory holds for transmission through scattering media as well. Due to the fine changes in surface structure, the reflected light interferes with itself and the measured intensity is a random set of bright and dark spots. Figure 2-3 shows an example of speckle pattern. A wonderful review of speckle theory can be found in a book by Goodman [28].

Speckle is modeled as an infinite sum of random phasors. As a result, the intensity in each pixel (which is the absolute square of this infinite sum) is an exponentially distributed random variable, such that the probability to measure an intensity I is [28]:

$$P(I) = \frac{1}{\bar{I}} \exp\left(-\frac{I}{\bar{I}}\right) \quad (2.3)$$

where \bar{I} is the distribution mean (can be correlated to system parameters such as exposure time, source intensity, imaging geometry, etc.). Another important parameter

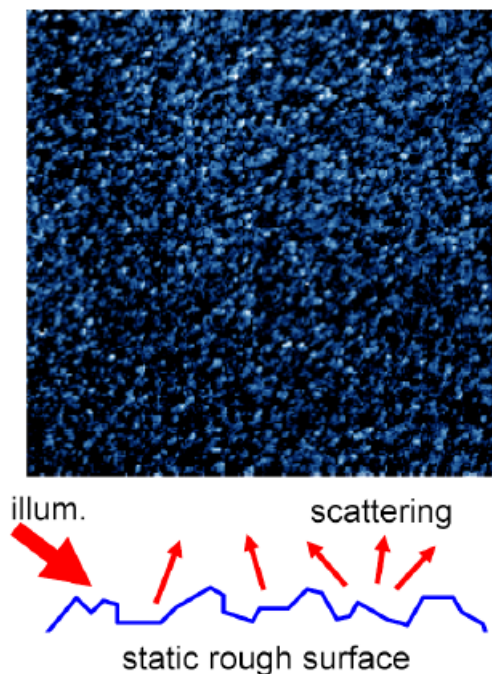


Figure 2-3: Speckle formation from a rough surface.

is the size of each speckle grain, which is a function of the imaging system aperture (larger aperture results in finer grains and vice versa).

Traditionally, speckle is considered an unwanted phenomena [82, 58]. However, since speckle encodes information about the surface, it can be used in effective ways [75] such as analysis of microstructure dynamics [10], vehicles velocimeter [3], surface tampering detection [18], tracking [105], and blood flow analysis, which will be discussed extensively in section 2.5 below and in chapter 4.

The remaining related works are grouped into methods to overcome scattering and methods to use coherent scattering for blood flow imaging.

2.4 Methods to Image through Scattering

Different methods to overcome scattering use various properties of electromagnetic radiation. This subsection is grouped accordingly.

- **Phase-Conjugate and Time Reversal**

The fundamental concept here is time reversal (a form of energy conservation),

which enables the reversal of scattering. As an illustrative example we can think of an object hidden behind a diffusive media; the object is illuminated by a plane wave, followed by a distortion of the wavefront by the diffuser. The distorted wavefront is recorded. If we send a conjugate of the distorted wavefront into the medium we will reconstruct the object. This is essentially some sort of holography, and indeed many early works used holography techniques to overcome scattering [27, 54, 51], and some still do [85].

Modern methods use spatial light modulators (SLM) to recover the wavefront. There are several advantages to using an SLM, such as no need for a reference beam and using an all-digital system. Recent works [92, 47] demonstrate focusing light into scattering media. By using the memory effect [22] of speckle, the method allows for imaging within a narrow field of view [62]. The method can work with incoherent light (although narrowband source results in better contrast) [49]. It was also shown that this technique can be employed in reflection mode with fluorescing markers [48].

One of the biggest advantages of this method is resolution. Since the scattering is completely rejected, it enables diffraction limit resolution. The main limitation is its relatively long and complicated optimization process (which requires a relatively constant medium). In order to get good results, it is preferred to use a coherent source. Finally, imaging based on the memory effect is limited to a very narrow field of view.

- **Speckle Correlations**

An interesting property of speckle is its auto-correlation function, which is almost a dirac delta. Calculating the auto-correlation of a speckle pattern with itself will result in a delta function. Since the hidden scene is multiplied by the speckle pattern, performing auto-correlation will result in the auto-correlation of the hidden scene (since it is convolved with a delta). Using different algorithms for phase recovery allows resolving the hidden scene from its auto-correlation [4]. A more recent work shows that this method can work with a single high

resolution image [46]. While this method is simple, it is very limited to thin diffusers.

- **Optical Coherence Tomography (OCT)**

OCT [40] is based on interference between the signal reflecting from the scene and a reference beam. Changing the reference beam allows scanning through different depths and rejecting reflections from other layers. Thus, OCT enables three dimensional imaging by scanning in a spatial plane using a focused light beam, and using interferometric localization in the depth axis. The technique enables creating a three dimensional image of a tissue by measuring it point by point (or line scanning). It is common to use either a short laser pulse or a partially coherent source. The analysis can either be performed in the time or frequency domain. Standard methods are capable of achieving resolution in the order of micrometers. OCT is commonly used in retinal imaging, lesion analysis (after the lesion has been removed from the body), etc.

- **Guidestar**

The idea of using guidestars goes back to astronomy and adaptive optics. The intuition behind it is to have some reference to provide information about the scattering process. In tissues, it is primarily done with ultrasound. Since ultrasound does not scatter in tissue it can be focused in deep tissue. Due to the acousto-optic effect [59, 98], when light passes through the ultrasound focus it is modulated (frequency shift). Only the modulated light is measured (for example using holography), and thus the optical contribution is only from within the ultrasound focus [102]. The main advantage of this method is the ability to focus deep into tissue (with ultrasound focus resolution). However, this method requires a combination of two systems, and it requires to raster scan the ultrasound focus in order to resolve the scene.

- **Photoacoustic Tomography**

When light is absorbed in tissue, it creates a thermally induced pressure wave

which can be detected using an ultrasound detector. The resolution of this technique decreases with depth at a rate of $1/200$ and can reach upto 7cm deep [100]. The main advantages of using photoacoustic methods is the ability to resolve optical contrast in ultrasound depths (order of cm). Yet, this method is based on coupling of two systems, and is limited to absorption analysis.

- **Time Gating**

Since ballistic photons do not scatter, they can be used to image absorption within a medium in transmission mode (this is the fundamental concept behind x-ray imaging). Because the ballistic photons are the first to arrive, it is possible to time gate the imaging sensor such that only ballistic photons are used for imaging. Hardware used for time gating includes a streak camera [103] and Kerr gate [96]. The main limitation of time gating is SNR, since only a few photons propagate without scattering.

- **Global-Direct Separation**

Global-direct separation is a ray-based method that aims to decouple rays that undergo a different number of bounces in a scene [66]. The direct component is a result of a single bounce, while the global component includes higher order terms such as sub-surface scattering and inter-reflection. It has been shown [66] that high frequency illumination can be used to separate the global and direct components. This method has been recently enhanced [30, 50]. A complementary method [69] demonstrated a hardware-based global-direct solution using dual coding. Achar [1] addressed the issue of moving objects during global-direct separation by registering frames captured with high frequency illumination patterns. Global-direct separation was used in medical imaging for enhancing veins in skin imaging [44].

- **Time-Resolved**

Time resolved imaging is a method that aims to capture extremely high FPS

movies, which capture the dynamics of light scattering in a scene. As opposed to time gating, time-resolved methods aim to use diffused photons as well as ballistic photons. Results include "light in flight" using a streak camera [35, 93] and using a SPAD array [25]. The use of a streak camera enabled imaging behind a corner [94, 31]. Streak camera was also used for lensless imaging [68] and estimating surface BRDF [64, 65]. More recently it was shown that time-resolved measurements can be used to recover albedo of patches hidden behind a diffuser [63], as well as to estimate pose of shapes behind a diffuser [76]. Other modalities to capture time-resolved information include avalanche photo-diodes (APD), which was used to reconstruct a scene through a pin-hole [43]. While all methods mentioned here are based on pulsed sources (i.e. measurement of a scene to an impulse in time), other methods for time-resolved measurements are based on frequency domain (known as time-of-flight cameras) which were also used for imaging through scattering [34] and behind corners [33, 45].

- **Diffuse Optical Tomography (DOT)**

DOT is based on the diffusion model of light. It is based on a set of sources and detectors. According to the diffusion equation, each source will generate light-tissue interaction within a given volume, and each source will measure this contribution from a specific volume. The measured light is the sum of all optical paths within the sample. Most techniques use frequency modulation of the light source and solve the diffusion equation in frequency domain. The penetration depth can be controlled by modulating the illumination and using various wavelengths. From a mathematical perspective, illuminating the scene from multiple points and measuring multiple points provides boundary conditions for the Helmholtz equation and allows solving the tomography problem, which results in a three dimensional tissue reconstruction [6, 26]. Recent studies also perform tomographic reconstruction of fluorescence lifetimes [38].

2.5 Imaging Blood Flow Speed with Laser Speckle Contrast Imaging (LSCI)

The use of laser speckle for blood flowmetry was suggested by Briers and Fercher [23] in 1981. Originally the method was used for analysis of retinal blood flow, where it was suggested that analysis of the speckle contrast provides extra information on the scene. The use of laser speckle contrast for flow analysis has many terms: Laser Speckle Contrast Imaging (LSCI), Laser Speckle Imaging (LSI) [86] and Laser Speckle Contrast Analysis (LASCA).

There are different types of blood flow analysis using speckle; they differ in the size of blood vessels and location in the body. Earlier work concentrated on blood vessels in the retina [23] and later evolved to skin perfusion (capillary vessels) [9] and large microvascular networks [60, 13, 53, 55]. Analysis of wound healing in pigs was performed recently [87]. Commercial devices [72] exist for medical use.

There has been a lot of work to model and extend speckle formation for quantitative flow analysis [19, 24, 28, 104], but deriving rigorous quantitative results remains an open question [19]. Advancements have included dual-wavelength systems for studying microvascular activity in burns [74], and multiple exposures in order to use speckle temporal statistics for improving spatial resolution [14] or contrast of cerebral flow through the skull [55]. Rege et al. suggest anisotropic numerical processing for increased SNR [78].

Doppler-based methods are alternatives to LSCI. In Doppler-based methods, the Doppler shift of scattered light is measured and correlated to speed. Briers, however, showed that LSCI and Doppler methods are equivalent [8], except that LSCI has better sensitivity at low speeds, and that Doppler methods account for multiple scattering. A recent work [24] uses laser Doppler for flowmetry in skin and suggests a model for quantitative analysis. Doppler sensitivity has been improved in combination with ultrasound [97]. Quantitative comparison of skin perfusion measurements between a full field laser Doppler imager and a commercial device concluded that a multi-exposure device offers some advantages [89].

Chapter 3

Fluorescence Lifetime Imaging in Scattering Media

Imaging through scattering media is a pervasive problem in optics, as scattering precludes direct image formation. One way to overcome scattering is to reduce the problem from imaging to resolving information on the scene; for example, determining the presence or absence of an object, among a finite number of possibilities, is often sufficient for remote sensing applications. In the context of scattering, this suggests the use of fluorescing markers. Fluorescence has already been widely used in remote sensing [37], and it is also used in novel super-resolution methods such as STORM [79] and PALM [5, 36].

An important aspect of the fluorescence process is its time profile $R(t)$, which is usually modeled as a decaying exponential:

$$R(t) = \frac{1}{\tau} \exp\left(-\frac{t}{\tau}\right) \quad (3.1)$$

where τ is the fluorescence lifetime. This parameter can be a useful marker for *in vivo* imaging, and indeed it is widely used in fluorescence lifetime imaging microscopy (FLIM). The time parameter is important since it provides information on the environment of the fluorescing marker. Unfortunately, FLIM is limited to thin tissue layers, which impedes its use for whole body imaging [52].

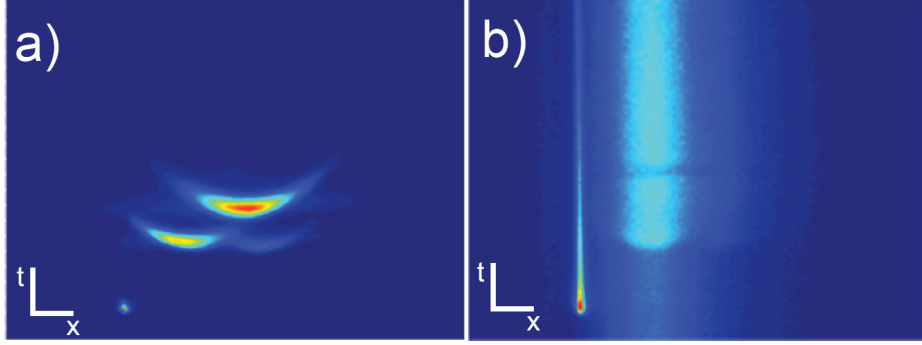


Figure 3-1: Sample fluorescence lifetime measurement with a streak camera. a) Set of 3 non-fluorescing patches hidden behind a diffuser. b) 2 fluorescing patches with decay times extending throughout the entire image (recorded without UV filter). The diffuser is fluorescent, noted by the decay of the calibration spot in the bottom left part of the images. Scale bars: 4.2 cm (horizontal), 200 ps (vertical).

In this chapter we suggest a novel wide-field method for localization and lifetime classification of fluorescing markers hidden behind a turbid layer [81]. The method is based on ultrafast measurements using a streak camera and a sparse-based optimization framework. This technique does not rely on coherence, and does not require the probes to be directly in line of sight of the camera, making it potentially suitable for long-range imaging.

3.1 Ultrafast Measurements Using a Streak Camera

In this work we use an ultrafast time-resolved measurement performed with a streak camera. A streak camera is a device that images a single line in space, each pixel on that line is measured in time with a $2ps$ time resolution. The result is a streak image where the y-axis of the image (rows) is the time axis. Fig. 3-1 shows the streak measurements of a set of fluorescing and non-fluorescing patches hidden behind a diffuser. In our system, the streak camera has $M = 512$ rows (i.e. a time window of $T_w = 1ns$) and $N = 672$ spatial pixels.

Our goal in the next section is to derive a mathematical model (forward model), which generates simulated streak measurements for patches hidden behind a diffuser.

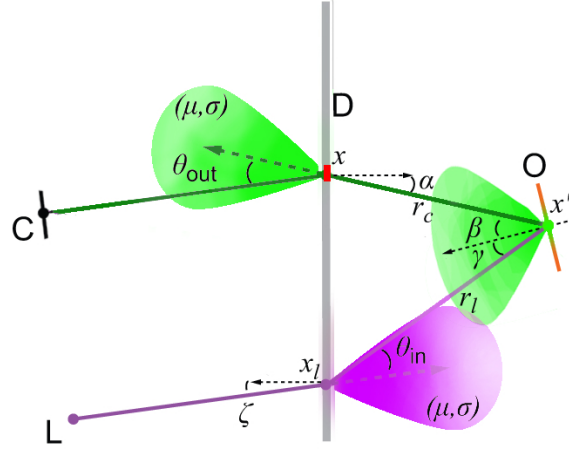


Figure 3-2: Geometry of diffuser and patch

3.2 Forward Model

To develop the forward model we consider the sketch shown in Fig. 3-2. Laser light (L) scatters through a diffuse layer (D) toward an object (O), which produces some response (R). Light then scatters back toward the diffuser and is imaged onto a time-resolved sensor (C). For a given incident laser pulse at position x_l with incident power of I_0 , the measured time-resolved image is given by [63, 94] :

$$I_l(x, t) = I_0 \int g(x_l, x, x') R(x', t) *_t \delta(t - c^{-1}(r_l(x') + r_c(x'))) dx' \quad (3.2)$$

where $*_t$ denotes convolution in time, $r_l(x') = \|x' - x_l\|$, $r_c(x') = \|x' - x\|$, and $g(x_l, x, x')$ is a time-independent physical factor that depends on the system geometry:

$$g(x_l, x, x') = \cos(\zeta(x_l)) N(\theta_{in}(x')) \frac{\cos(\gamma(x')) \cos(\beta(x')) \cos(\alpha(x'))}{\pi^2 r_l^2(x') r_c^2(x')} N(\theta_{out}(x')) \quad (3.3)$$

The angles $\{\alpha, \beta, \gamma, \zeta, \theta_{in/out}\}$ are defined by the geometry in Fig. 3-2. $N(\theta)$ is the diffuser scattering profile, characterized by a scattering width σ . The object response function R is generally a function of the reflectance (including, for example, the efficiency) of an object point, as well as a function of time. For fluorescing markers, the lifetime and efficiency can vary in space.

Here, each point in the object volume can contain a single but different exponential

decay (an extension to Eq. 3.1):

$$R(x', t) = \rho(x') \frac{1}{\tau(x')} \exp\left(-\frac{t}{\tau(x')}\right) u(t) \quad (3.4)$$

where $\rho(x')$ is the local time-independent reflectance, $\tau(x')$ is the local lifetime, and $u(t)$ is the unit step function, imposed to satisfy causality constraints. Note that the delta function confines intensity to a hyperbolic path in the $x - t$ plane: a streak image for a single point source (ignoring any time response in R) is a hyperbola (Fig. 3-3a).

For a single-shot image acquisition system, Eq. 3.2 is the recorded time-resolved image. However, for a pulse train (which is used experimentally to increase SNR), the fluorescent lifetimes must be compared with the repetition rate T of the illumination. If $\tau \sim T$, then the fluorescent decay from the current pulse is superposed with the decays from previous pulses. Quantitatively, if we model the illumination with a pulse train, the streak image becomes

$$I_l(x, t) = I_0 \int g(x_l, x, x') R(x', t) * \sum_{m=-\infty}^{\infty} \delta(t - c^{-1}(r_l(x') + r_c(x')) - mT) dx' \quad (3.5)$$

In order to analyze Eq. 3.2 with 3.5, we first assume no spatial dependency:

$$R(t) = \rho \frac{1}{\tau} \exp\left(-\frac{t}{\tau}\right) u(t) \quad (3.6a)$$

$$I(t) = R(t) * \sum_{m=-\infty}^{\infty} \delta(t - mT) \quad (3.6b)$$

such that:

$$I(t) = \sum_{m=-\infty}^{\infty} \exp\left(-\left(\frac{t-mT}{\tau}\right)\right) u(t-mT) \quad (3.7a)$$

$$= \exp\left(-\frac{t}{\tau}\right) \sum_{m=-\infty}^M \left(\exp\left(\frac{t}{\tau}\right)\right)^m \quad (3.7b)$$

$$= \frac{1}{1 - \exp\left(-\frac{T}{\tau}\right)} \exp\left(-\frac{T}{\tau} \left(\frac{t}{T} - \left\lfloor \frac{t}{T} \right\rfloor\right)\right) \quad (3.7c)$$

where $M = \lfloor t/T \rfloor$ (here $\lfloor \cdot \rfloor$ is the integer floor function). Adding the spatial dependency back to the equation we get:

$$I_l(x, t) = I_0 \int g(x_l, x, x') \frac{\rho(x') \tau^{-1}(x')}{1 - \exp\left(-\frac{T}{\tau(x')}\right)} \exp\left(-\frac{T}{\tau(x')} \left(\frac{t - c^{-1}(r_l(x') + r_c(x'))}{T} - \left\lfloor \frac{t - c^{-1}(r_l(x') + r_c(x'))}{T} \right\rfloor\right)\right) dx' \quad (3.8)$$

Here, we assume that there is only a small number of fluorescent particles in the field of view. Thus, we measure the fluorescence dynamics of discrete object points, located at coordinates x_j with lifetime τ_j :

$$I_l(x, t) = I_0 \sum_j g(x_l, x, x_j) \frac{\rho_j \tau_j^{-1}}{1 - \exp\left(-\frac{T}{\tau_j}\right)} \exp\left(-\frac{T}{\tau_j} \left(\frac{t - c^{-1}(r_l(x_j) + r_c(x_j))}{T} - \left\lfloor \frac{t - c^{-1}(r_l(x_j) + r_c(x_j))}{T} \right\rfloor\right)\right) \quad (3.9)$$

An example of simulating a single patch for the case of $\tau \rightarrow 0$ and $\tau = 5ns$ using Eq. 3.9 is shown in Fig. 3-3.

Eq. 3.9 is a time-periodic function. To gain some intuition, we ignore all spatial dependence and focus on the time dependence, plotted in Fig. 3-4 for a single fluorescent point. Fig. 3-4a shows the incident pulse train with repetition rate T . Compared to all other temporal parameters, the pulse duration can be considered

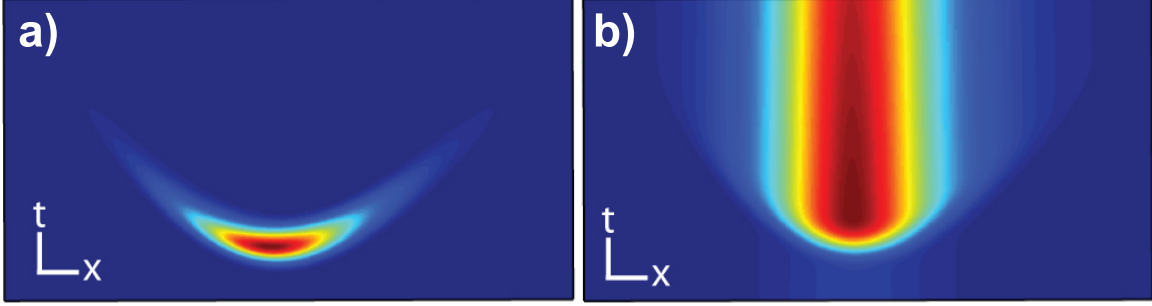


Figure 3-3: A simulated streak image for: a) a non-fluorescing patch, that is $\tau \rightarrow 0$, and b) a fluorescing patch with $\tau = 5ns$. Scale bar: 100ps (vertical) and 1cm (horizontal).

negligible. Fig. 3-4b shows the time response for $\tau/T = 0.40$ and $\tau/T = 2.56$, respectively. The dashed curves represent the individual responses to each pulse, and the solid curves represent the expected measurement. We see that for longer lifetimes, the contrast of the measured signal decreases due to the residual fluorescence from previous pulses. If we define the contrast V as the difference between the maximum and minimum intensity values divided by the sum:

$$V \equiv \frac{R^{(+)} - R^{(-)}}{R^{(+)} + R^{(-)}} \quad (3.10)$$

where we can use Eq. 3.7 to calculate the intensity right before and after the pulse:

$$R^{(+)} \equiv \lim_{t_\epsilon \rightarrow 0^+} R(t_\epsilon) = \frac{1}{\tau (1 - \exp(-\frac{T}{\tau}))} \quad (3.11a)$$

$$R^{(-)} \equiv \lim_{t_\epsilon \rightarrow 0^-} R(t_\epsilon) = \frac{\exp(-\frac{T}{\tau})}{\tau (1 - \exp(-\frac{T}{\tau}))} \quad (3.11b)$$

we find that

$$V = \tanh\left(\frac{T}{2\tau}\right) \quad (3.12)$$

Longer lifetimes, therefore, tend to increase the "dc" component of the signal relative to the high frequency edges. This is effectively a low pass filtering operation in time.

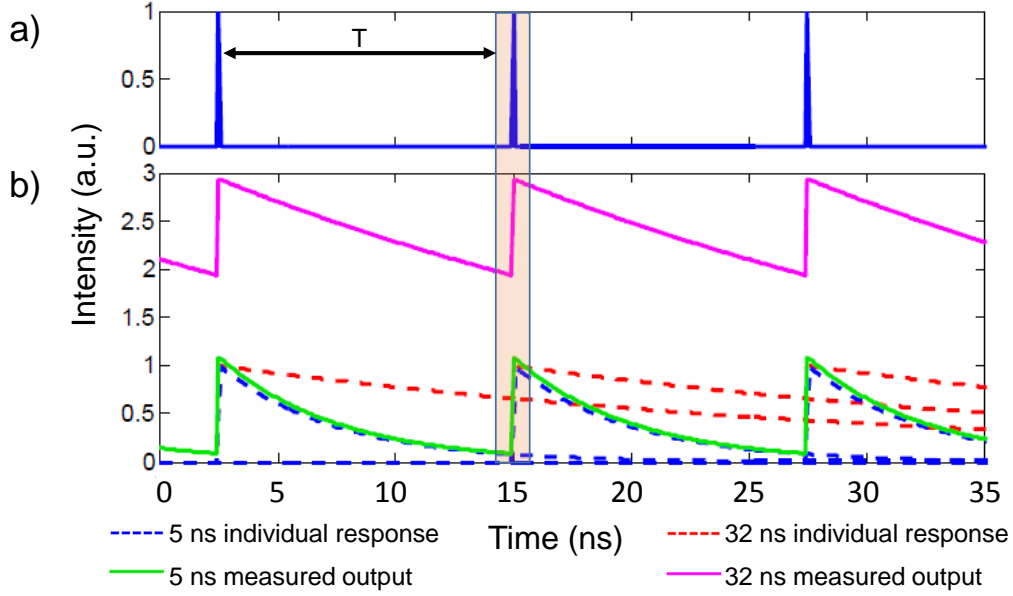


Figure 3-4: Time-resolved fluorescence imaging with a pulse train. a) Incident pulse train, separated by period T . b) Measured output for a fluorescing marker with lifetimes 5ns and 32ns . Dashed lines indicate the individual response for a single pulse. Solid lines indicate the measured signal. The orange box indicates detector time window.

In the next section we seek to answer the following question: given a set of time-resolved measurements $\{I_l\}_{l=0,1,\dots,L}$ (where different l corresponds to different illumination points on the diffuser), what are the locations $\{x_j\}$ and lifetimes $\{\tau_j\}$ of the fluorescent tags generating the signal?

3.3 Reconstruction Algorithm

In order to recover the unknown positions and lifetimes from a set of time-resolved measurements, we divide the problem into two steps. We first recover the objects' positions. Then, using the measurements and recovered positions, we classify the objects according to lifetimes.

It should be noted that the model in Eq. 3.9 is non-invertible, which makes this problem highly ill-posed. A sparsity constraint allows us to overcome the strong signal overlap. Note that this is the physical insight for subwavelength resolution using PALM [36] or STORM [79] microscopy and single pixel acquisition modalities

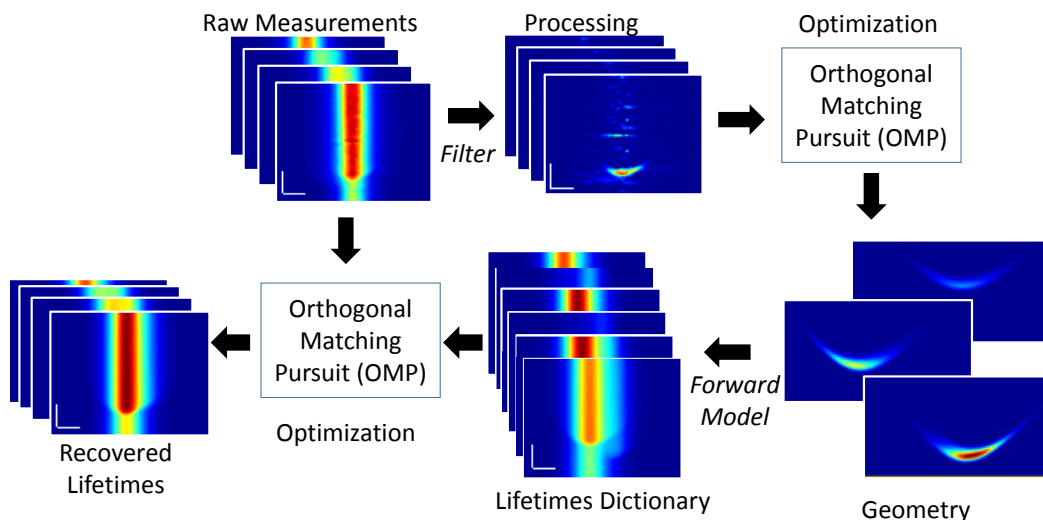


Figure 3-5: Reconstruction algorithm flow. Raw measurements are filtered to produce streak hyperbolas; geometry is recovered via OMP; a lifetime dictionary is created; and another OMP step identifies lifetimes of the probes.

[88]. Our extensions here offer similar possibilities in remote sensing.

The reconstruction flow is shown in Fig. 3-5. This two-step process allows us to exploit the sparsity of the geometry information by avoiding the signal overlap due to relatively long fluorescence decay times.

3.3.1 Step 1: Geometry Reconstruction

At the first step, we aim to localize the patches. Hence we'd like to remove the time blur which is due to the fluorescence profile. Ideally, the data could be deconvolved with an appropriate $R(x, t)$, but we do not know the individual lifetimes in advance. Instead, we operate on each streak image with a simple high-pass temporal filter (first order derivative) and zero all resulting negative values. The result is a set of streak images $\{I_l^{(F)}\}$ that contain (approximately) only the edge structures, and hence geometrical information.

We then define a measurement \bar{I}_l to be the vectorized form of a single time-resolved image $I_l^{(F)}$, i.e., \bar{I}_l is an $MN \times 1$ vector. We concatenate all L vectors into a single $LMN \times 1$ data vector: $I_{meas} = (\bar{I}_1^T \bar{I}_2^T \dots \bar{I}_L^T)^T$. This is a complete experimental

measurement.

Next, we define a vector I_p as the expected data from a single non-fluorescent object located at point x_p . We can create a dictionary matrix D whose columns consist of the expected data of all possible point locations and lifetimes: $D = (I_1 I_2 \dots I_P)$. Thus, for a set of object points with weights ρ , we can write the system in a vector-matrix form as

$$I_{meas} = D\rho \tag{3.13}$$

where the elements of $\rho = (\rho_1, \rho_2, \dots, \rho_P)^T$ are the reflectance values of each potential object point ($0 < \rho_P < 1$). Note that if the number of object points in the experiment is much less than the total length of ρ , then most elements of ρ are zero. Thus, we can recover the nonzero elements of this vector using a sparsity-promoting algorithm. The positions of each nonzero element in ρ determine the location of the object points. We seek to solve the following optimization problem:

$$\text{Minimize } \|\rho\|_0 \quad \text{subject to} \quad \|I_{meas} - D\rho\|_2 < \epsilon \tag{3.14}$$

where $\|\cdot\|_0$ is the l_0 norm which equals the number of nonzero elements in ρ , and ϵ represents an error tolerance due to noise.

To build the dictionary matrix D , we simulate (via Eq. 3.9 with $\tau \rightarrow 0$) the expected streak images for a single non-fluorescing patch, and computationally scan its location throughout the working volume (Fig. 3-6).

Eq. 3.14 is solved via orthogonal matching pursuit (OMP) [71] to yield the dictionary atoms (or unit cells) that are best correlated with the filtered streak images. OMP is a greedy algorithm, which searches sequentially for the best atom that matches the input, subtracts its contribution from the data, and iterates this process until the residual error derivative is below a user-defined threshold. The number of iterations equals the number of objects recovered.

At the end of this stage we have recovered a set of possible patch locations. We note that due to the noisy input into the OMP step we often recover too many

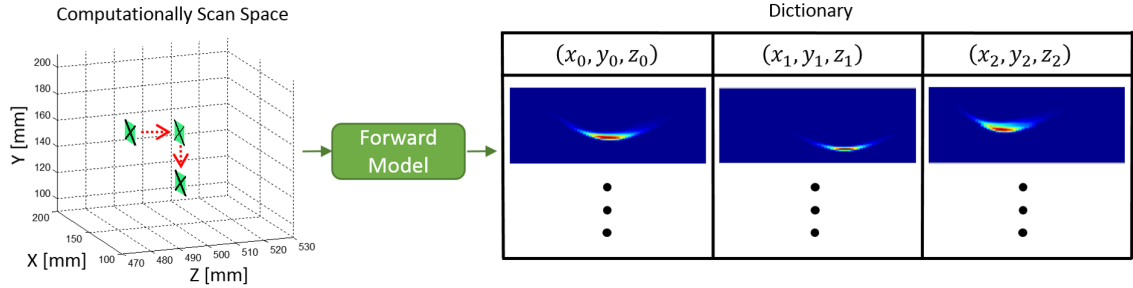


Figure 3-6: Dictionary construction flow. A patch is computationally moved in the interest volume to generate the corresponding L streak images which are vectorized in the dictionary columns. The column number corresponds to specific patch locations in the volume.

locations. This is resolved during the second step (see more information on the OMP algorithm stopping criteria below).

3.3.2 Step 2: Lifetime Reconstruction

With the locations of all patches recovered in the first step, we move on to the second step and render all possible florescent images using a known set of potential lifetimes. For N_p possible locations and N_f potential lifetimes, there are $N_p N_f$ atoms in this new fluorescent dictionary (the response is simulated using Eq. 3.9).

The fluorescent dictionary and the measured (unfiltered) fluorescent data are input into another OMP iteration, at the end of which the correct locations are picked up as well as the corresponding lifetimes.

3.3.3 OMP Stopping Criteria

The stopping criterion in the first step was chosen in order to make sure all the correct atoms are included in the first step, even if incorrect atoms are temporarily selected in the process. This is important since the second OMP step is based on the selection from the first step and cannot add new atoms. The first step in our method can be thought of as online dictionary generation, which generates all plausible locations. This stage is robust as long as the number of constructed atoms is significantly larger (about 3-5x) than the actual number of patches, and that is why we have chosen a

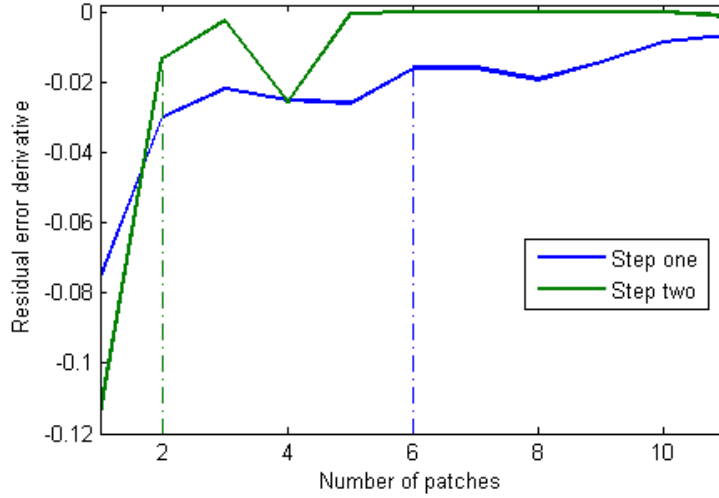


Figure 3-7: Residual error decrease rate versus number of patches considered in the OMP solution. The dashed lines represents the location in which the stopping criterion has reached.

relaxed criterion.

The second stage requires a more gentle care, as the number of atoms is not known a priori. This stopping criterion is a known problem with no closed-form solution once noise appears. Our algorithm handles this limitation by monitoring the residual energy decrease rate, which provides information on the correct number of patches. Fig. 3-7 demonstrates this; we note that the residual error of the first step decreases slowly, while in the second step the error decreases very fast and reaches almost zero at the correct number of patches. Needless to say that if we know the number of patches, any search procedure can be used.

Specifically in our algorithm we use the residual error derivative as a measure and empirically select a threshold of -0.02 as a stopping criterion.

3.3.4 Algorithm Parameters

The geometry dictionary resolution is chosen to be $dx = 6.9mm$, $dy = 7.5mm$, $dz = 5.2mm$. The volume of interest results in 18856 atoms in the dictionary. Therefore, using the full resolution streak images results in a vector of size $12 \times 512 \times 672 = 4128768$. Storing the full dictionary requires approximately 622GB of memory. By

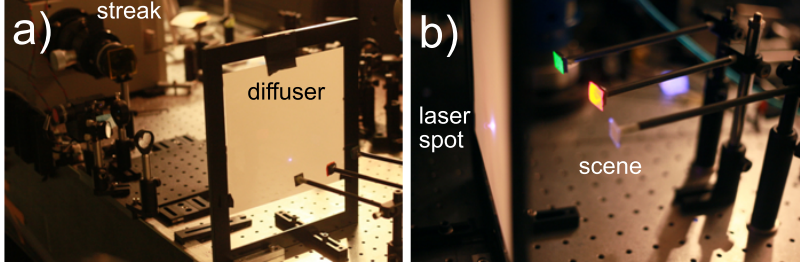


Figure 3-8: Experimental geometry. a) Experimental setup. b) Scene under investigation.

down-sampling each image to 51×67 pixels, a vector length of 41004 is obtained for the 12 images, which results in dictionary size of $6.2GB$. This is a factor of 100 reduction in computational burden. Another approach that might be considered is the use of sparse representation; however, since the dictionary structure is highly irregular, this approach is not beneficial. The lifetime dictionary is far smaller than the geometry dictionary, which allows us to use full resolution images. Using an unoptimized MATLAB code and a desktop computer (Intel Core i7 with $32GB$ RAM), it took the algorithm 91 seconds per reconstruction on average.

3.4 Experimental Demonstration

The scene is a set of three $1.5 \times 1.5cm^2$ square patches hidden behind a diffuser, shown in Fig. 3-8. The first patch (NF) is non-fluorescent. The second patch (QD) is painted with a quantum dot solution ($\tau = 32ns$) [12]. The third patch (PI) is painted with Pyranine ink ($\tau = 5ns$) [70].

We carry out three experiments, each with a different patch configuration. Each column in Fig. 3-9 corresponds to a different configuration. Fig. 3-9a shows the experimental measurements. For each configuration, we input the filtered data (Fig. 3-9b) into OMP to recover the location of each patch. After reconstructing the lifetimes, we use the forward model (Eq. 3.9) to generate streak images that match the measurements (Fig. 3-10a). The reconstructions are shown in Fig. 3-10b. Because we use a UV filter, no information from the NF patch is recorded. We note that the fluorescent lifetimes are always identified correctly, and that the position error is on

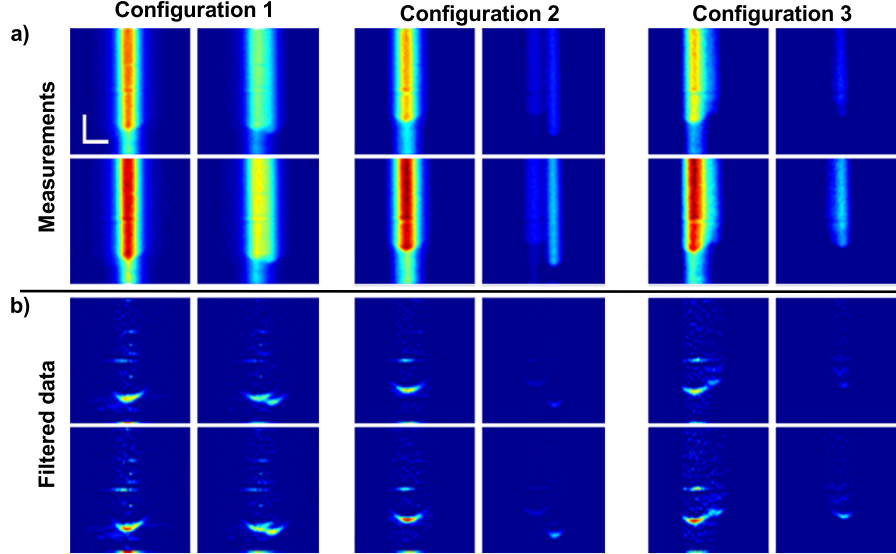


Figure 3-9: Experimental measurements as input to the algorithm. Each column is a different configuration, and for each we show a) example of four measurements taken and b) the corresponding high-pass filtered images. Scale bars: 4.2cm (horizontal), 200ps (vertical). The four points correspond to measurements with illumination positions x_{12} , x_{11} , x_9 , x_8 as shown by the labels in Fig. 3-11.

| | Configuration 1 | | | | Configuration 2 | | | | Configuration 3 | | | |
|-------|-----------------|------------|------------|--------------|-----------------|------------|------------|--------------|-----------------|------------|------------|--------------|
| Patch | ΔX | ΔY | ΔZ | $\Delta\tau$ | ΔX | ΔY | ΔZ | $\Delta\tau$ | ΔX | ΔY | ΔZ | $\Delta\tau$ |
| QD | 8.1 | 9.9 | 1.6 | 0 | 5.8 | 14.6 | 1.67 | 0 | 4.8 | 7.0 | 2.6 | 0 |
| PI | 5.7 | 10.9 | 1.6 | 0 | 2.4 | 14.3 | 2.13 | 0 | 6.9 | 16.7 | 1.7 | 0 |

Table 3.1: Reconstruction error. The numbers represent distances from the center of each ground truth patch in space to the center of the corresponding reconstructed patch (length units are millimeters).

the order of the patch size or dictionary resolution (table 3.1). Finally, because we assume only a finite number of lifetimes, the algorithm distinguishes between the PI and QD patches with no errors. We emphasize here that the reconstruction is spectrally invariant, so that two patches with the same emission wavelength can still be separated.

3.4.1 Optical Setup

The experimental setup is shown in Figs. 3-8 and 3-11. A Titanium:Sapphire laser (1.15W ($\sim 15\text{nJ/pulse}$), $\lambda = 800\text{nm}$, $T = 12.5\text{ns}$ repetition rate, and 50fs

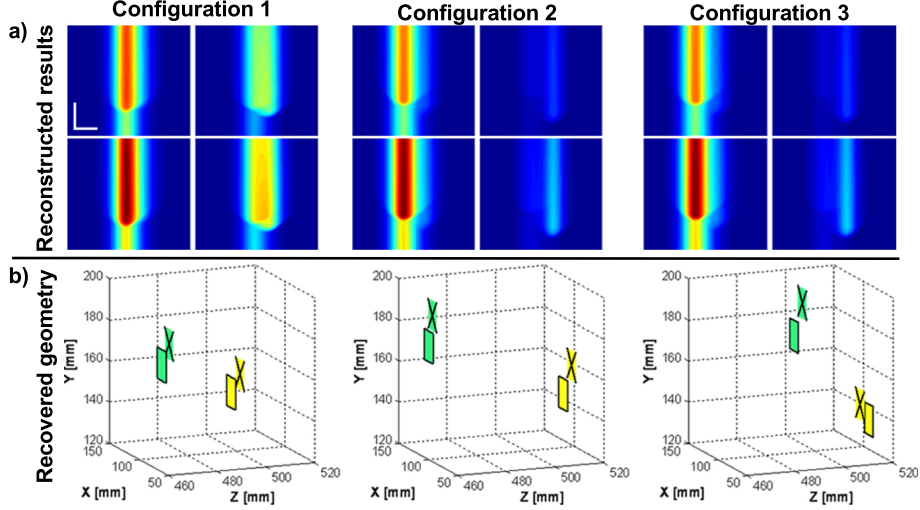


Figure 3-10: Reconstruction results. a) Reconstructed streak images using the recovered locations and lifetimes. b) Geometry recovered for each configuration. Green and yellow correspond to PI and QD patches, respectively. Patches with an X are the recovered locations; solid outlines indicate ground truth (measured by a Faro Gage Arm).

pulse duration) is frequency-doubled using a barium borate (BBO) crystal to $400nm$ and is then focused ($\sim 100mW$ average power at the focus) onto a $0.7mm$ thick polycarbonate diffuser (Edmund Optics, 55-444) with a Gaussian diffusion profile $N(\theta) = \exp(-\theta^2/2\sigma^2)$ where $\sigma \sim 60^\circ$. Light is scattered toward a scene, which scatters light back toward the diffuser, the front side of which is imaged onto a streak camera (Hamamatsu C5680) with a time resolution of $2ps$ and a time window of $1ns$. The detector has a one-dimensional aperture and records the time profile of a horizontal slice of the diffuser, with an $x-t$ resolution of $M \times N = 672 \times 512$ pixels. To increase SNR, the total exposure time is $T_{int} = 10ms$, so that a given streak image integrates light scattered from T_{int}/T incident pulses. Because the streak camera has only a 1D horizontal aperture, we scan the incident laser position across $L = 12$ positions to mimic a 2D aperture [83] and record 12 streak images. The total acquisition time is approximately LT_{int} .

To calibrate intensity fluctuations and temporal jitter, a portion of the incident laser beam is split off and focused onto the diffuser, directly in the view line of the camera, so that a streak image of a direct reflection is observed. This calibration

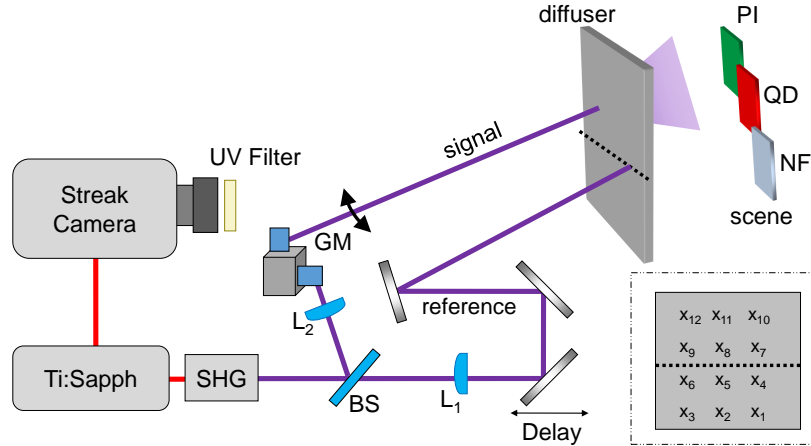


Figure 3-11: Experimental setup. A 1.15 Watt Ti:Sapphire beam is frequency-doubled and is focused onto a diffuser via a pair of galvo mirrors (GM), which scan the beam across the diffuser to different incident positions (inset). Light is scattered by various objects and is recorded by a streak camera (field of view indicated by the dotted line). A fixed reference beam is used to correct intensity and timing noise. Inset: locations of incident laser positions for each streak image.

spot is fixed for the duration of the acquisition of all streak images (incident laser positions) and is used to subtract any timing jitter noise in the detector and to scale any intensity fluctuations. The calibration point is then cropped to reduce errors during the reconstruction process.

Fluorescing Markers Parameters

The scene is a set of three $1.5 \times 1.5 \text{ cm}^2$ square patches (Fig. 3-8b). The first patch (NF) is non-fluorescent, cut from a white MacBeth Colorchecker square. The second patch (QD) is painted with a CdSe-CdS quantum dot solution ($\tau = 32 \text{ ns}$, $\lambda_{\text{emission}} \sim 652 \text{ nm}$) [12]. The third patch (PI) is painted with Pyranine ink ($\tau = 5 \text{ ns}$, $\lambda_{\text{emission}} \sim 510 \text{ nm}$) [70]. To study the time-resolved scattering of both the UV excitation (400 nm) and the fluorescent emission (652 nm from QD and 510 nm from PI), images are recorded both with and without a UV cutoff filter ($\lambda_{\text{cut}} = 450 \text{ nm}$). The UV filter eliminates the UV reflection from the patches and with it only the visible fluorescence emission profile is captured by the camera (e.g., Fig. 3-1b). A non-fluorescent analog is shown in Fig. 3-1a. Only images taken with the UV cutoff filter are used for

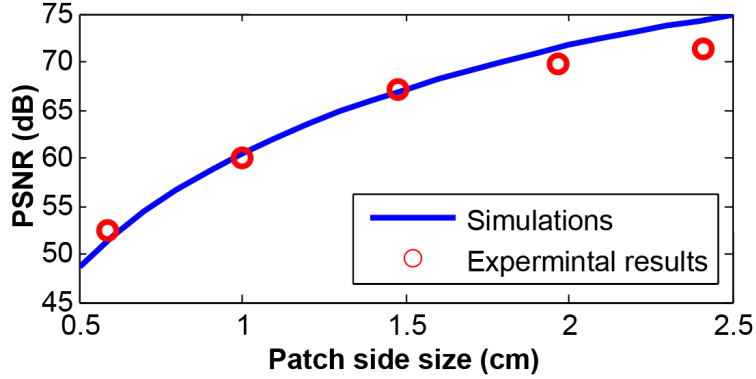


Figure 3-12: Patch size effect on PSNR. The red dots are experimental measurements (taken with fixed exposure and gain), and the blue curve is a forward model simulation prediction (to simulated measurements we add white Gaussian noise with variance that matches the measured variance).

reconstruction, thus information for the NF patch is not measured. While each of these probes has several main absorption bands, the closest dominant absorption maxima for QD and PI are at $600nm$ and $460nm$ respectively [12, 73]. Therefore $400nm$ illumination can properly excite the probes into fluorescent mode.

3.5 Noise and Sensitivity Analysis

In our system, changes in the size of the patch behind the diffuser affect the PSNR as in Fig. 3-12. The red markers are measured data and the blue curve is the result of our forward model. For each image we estimate the noise by using the algorithm described in [57]. While the signal strength increases with the patch size, the estimated noise levels in all five measurements are identical (within 1.5% of the noise mean). As expected, the PSNR improves for larger patches. Note that the measured PSNR of the largest patch is slightly lower than what is expected according to the forward model; this can be explained by non-linear behavior of the streak tube dynamic range near the saturation level of the sensor.

Based on the effect of patch size on PSNR, the reconstruction error is also indirectly a function of patch size. To understand the effects of noise, we analyze the reconstruction accuracy as a function of both measurement noise and patch size (Fig.

3-13). Twelve time-resolved images are simulated (via Eq. 3.2) using three different fluorescent objects, with white Gaussian noise added to the images. These images are then input into the reconstruction algorithm.

Fig. 3-13a shows the reconstruction error as a function of the noise level and patch size. The plotted error is a sum of all three distances between the reconstructed objects and the corresponding ground truth locations of fluorescing patches divided by the diagonal size of dictionary voxel. The error results show three step-like changes for all patch sizes (Fig. 3-13a); as the patch size increases the signal level increases, and the first jump in error is postponed to larger added noise. It should be noted that for all simulations we used the original dictionary designed for $1.5 \times 1.5 \text{cm}^2$ patches.

We see that for low noise variance the error is virtually zero. As noise increases, step-like jumps in the error are noted. At first, this seems counter-intuitive: we expect the error to increase continuously with noise. However, the discontinuities occur as a result of the sparsity-based method.

At specific noise levels, OMP cannot distinguish between different curves, and so an atom is essentially lost (Fig. 3-13). This occurs at thresholds when the energy of the lost atom is comparable to the noise level. After this threshold, the algorithm selects a different (incorrect) atom that overlaps with one of the remaining, stronger atoms (transitions from II to III and from III to IX). When the last atom is lost (point X), the algorithm chooses the atoms with the largest foot print. Similar analysis for choosing the patches' lifetimes showed that the lifetime estimation is even more robust to noise.

3.6 Accessible Volume

As seen from the reconstructions presented in Fig. 3-10, the patches are not required to be directly in the line of sight of the camera; therefore, unlike a conventional imaging system with a field of view (FoV), we need to define an accessible volume (or visible volume) for this imaging system (Fig. 3-14a and Fig. 3-14b). Because there are two sequential scattering events before the signal reaches back to the diffuser, the

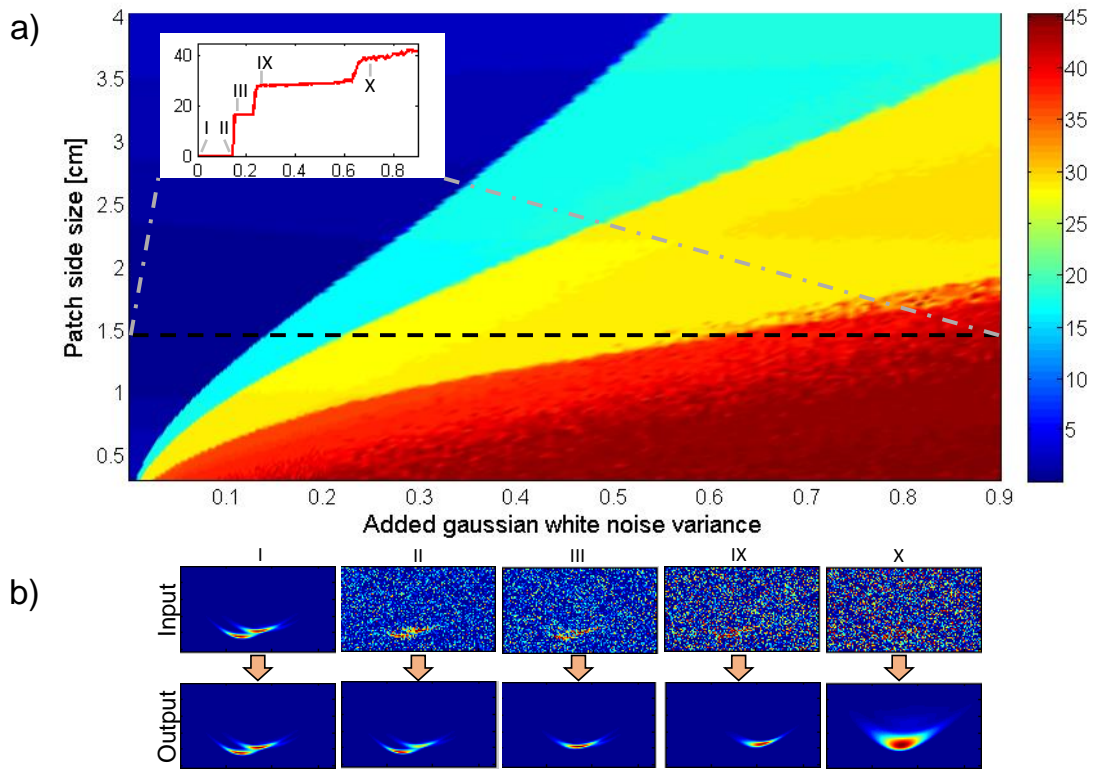


Figure 3-13: Noise performance. a) Analysis of reconstruction error as function of patch side size and added noise. White Gaussian noise with increasing variance (x-axis) is added while increasing the patch's size (y-axis). The color represents the total algorithm reconstruction error in arbitrary units. Inset figure shows the algorithm sensitivity along the black dashed line (corresponding to patch size of 1.5cm). b) Examples of different points on the inset graph which show input images with added noise and the reconstruction results. These images correspond to one of the twelve illumination points.

detected signal must fall off as the product of the square of the distances r_c and r_l . Assuming $r_c \sim r_l = r$, we have $I_l \sim I_0/r^4$ (Eqs. 3.2 and 3.3). Therefore, a larger accessible volume is obtained at the expense of lower SNR. The intensity from the closest object point (r_{D1}) should be within the dynamic range of the camera to avoid saturation:

$$KI_0 (r_{D1}^{-4}) \leq I_{sat} \quad (3.15)$$

where K is a constant that is inversely proportional to σ (the scattering angle of the diffusive layer). Also, the signal from the farthest point must be above the noise floor:

$$KI_0 r_{D2}^{-4} \geq I_{noise} \quad (3.16)$$

We can write these conditions as:

$$\left(\frac{KI_0}{I_{sat}}\right)^{\frac{1}{4}} < r < \left(\frac{KI_0}{I_{noise}}\right)^{\frac{1}{4}} \quad (3.17)$$

This gives us the intensity constraints on the maximum potential accessible volume (Figs. 3-14a,b). Further, the scattered light from all points must arrive within the sensor's time window T_w : $(r_c + r_l)_{max} - (r_c + r_l)_{min} < cT_w$. Thus, for a given incident laser position x_l , the accessible volume is the intersection of the volumes given by this time constraint and the intensity constraints (Fig. 3-14b). Note also that this volume is trimmed if σ is less than 90° .

Lastly, the number of illumination points L controls the total visible volume, which is the concatenation of L volumes described above for each laser position x_l . Further, for a scattering angle less than 90° , there can be gaps in the accessible volume close to the diffuser (Fig. 3-14c). Overall, increased scattering increases the accessible volume close to the diffuser. Therefore, the ability to reconstruct images is thus a competition between SNR, which is reduced by scattering, and the accessible volume, which is enhanced by it.

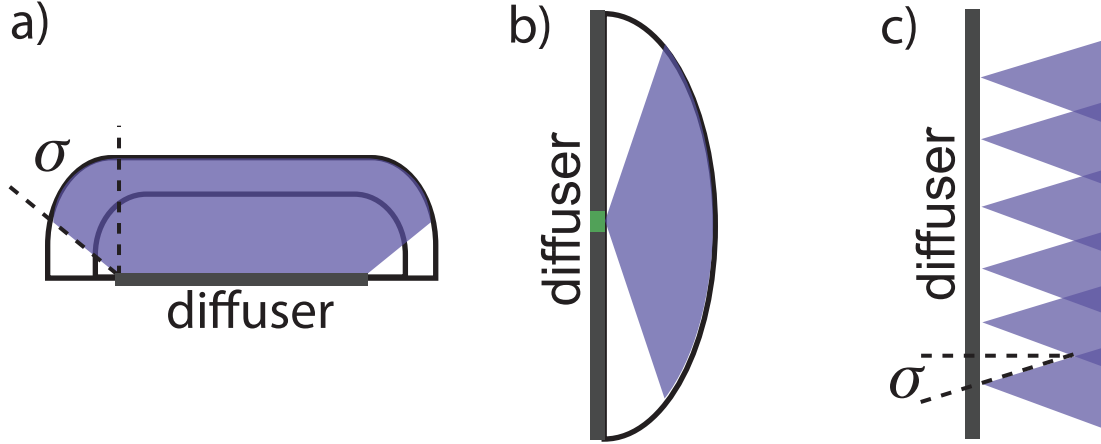


Figure 3-14: Visible volume. a) Top and b) side views of visible volume. The inner black curve shows the saturation bound, and the outer black curve shows the noise-limited bound. The purple area shows the geometry limitation imposed by diffusion/scattering angles (σ). The green rectangle in the middle of the diffuser is the line imaged by the camera (conventional FoV). c) Illumination gaps due to small scattering angles and widely-spaced illumination points.

3.7 Comparison to Previous Methods

Our method is compared to other existing methods in table 3.2. To the best of our knowledge, only fluorescence diffuse optical tomography (FDOT) [38] is capable of recovering fluorescence lifetime and localizing patches. However, it requires more acquisition steps (full rastering of the sample), and direct positioning of fluorescent probes in line of sight of the detector, since it is based on transmission mode; it also depends on ballistic photons. It is noteworthy that a simple optimization [63] and back-projection technique [94] for localizing fluorescent tags would fail because of the significant lifetime of the fluorescent tags; hence a streak-based method with use of a dictionary-based algorithm is needed to simultaneously reconstruct both.

In order to compare the number of acquisition steps, we counted the number of required images for each method. In the case of FDOT [38], there are $84 \times 46 = 3856$ required measurements with an ICCD. In the case of [49], the required number of images is equal to the number of optimization steps, which is a multiplication of the spatial light modulator resolution (in the order of 600×600) and the number of phase steps.

| | Reconstruction model | Fluorescence lifetime recovery | Recovery scale | Acquisition raster steps | Mode - Number of scatterings |
|--|--|--------------------------------|----------------|--------------------------|------------------------------|
| a. Our approach - (streak-based localizing fluorescent tags through diffuser) | Sparsity-based dictionary | Yes | Macro | 12 | Reflective-3 |
| b. ICCD-based fluorescence diffuse optical tomography | Ballistic photons-Standard convex optimization | Yes | Macro | 3856 | Transmissive-1 |
| c. Streak-based albedo recovery through diffuser | Standard convex optimization | No | Macro | 16 | Reflective-3 |
| d. Streak-based looking around the corner | Back projection | No | Macro | 60 | Reflective-3 |
| e. Spatial light modulator - based method | Adaptive wavefront correction | No | Micro | <600×600× phase steps | Transmissive-1 |
| f. Speckle-based approach | Using memory effect and speckle statistics | No | Micro | 10 | Reflective-1 |

Table 3.2: Comparison between different methods: a. our method, b. FDOT approach [38], c. streak-based with simple optimization [63], d. streak-based with back propagation [94], e. SLM-based [49] and f. speckle correlation approach [46].

As seen in table 3.2, our method is the only one that offers simultaneous 3D location and lifetime estimation in reflective mode after three consequent scattering events. This is crucial for recovering the patches that are not directly in front of the camera, but their fluorescent emission can reach the camera lens in the time window of the acquisition. The non-invasive reflective mode also makes our method more appealing for applications that require deeper localization of the fluorophores.

3.8 Discussion

Currently, we are modeling turbulence by scattering layers. This is common [90], but can be extended to thick media, provided the temporal blurring due to multiple scattering still allows us to resolve the fluorescence rise time via filtering. Theoretically, there is no fundamental limit precluding the extension of our method to volume scattering. The main issues are practical, namely, a reduction in SNR with an increase in complexity in forward modeling. However, the sparse prior we exploit here can alleviate these constraints. Since fluorescence signals are commonly sparse in nature, sparsity is a natural way to avoid local minima during reconstruction (as would occur in standard optimization methods) and to achieve a robust solution relatively quickly (i.e., in minutes rather than days). It is specifically the sparse prior that allows reconstruction in the presence of long lifetimes over narrow time windows. Our system offers wide field of view and does not rely on coherence. With our method, the relevant parameters are the diffusion constant, thickness of the diffuser, and the system time resolution.

Because the illumination intensity at the excitation wavelength is stronger than the emission, without a UV filter we can filter out the fluorescence and use only the geometrical information (including non-fluorescent objects) in the first OMP step. This results in higher reconstruction accuracy, but requires twice the recording time.

The underlying limits of the system are SNR and the accessible volume. One straightforward way to alleviate this for remote sensing applications is to increase the laser power. This can be done provided it is not harmful to the targets under study, so it is preferable to use the minimum laser power (lowest SNR) that still enables correct reconstruction.

In summary, we demonstrated time-resolved inversion of scattered light to locate fluorescent tags behind diffusive layers in wide-angle scenes and to identify their lifetimes. This technique, which relies on sparse optimization, has potential applications in remote sensing of spectrally identical fluorescent tags, and offers algorithmic benefits for fluorescence lifetime tomography beyond the conventional line of sight.

Chapter 4

Blood Flow Speed Measurement with Coherent Scattering

The use of coherent scattering (which results in speckle) for blood flowmetry was suggested by Briers and Fercher [23] in 1981. Originally the method was used for analysis of retinal blood flow, and later evolved to measure bloodflow speed in skin [9].

The process of blood flow into tissue is called perfusion, and it is a useful marker to measure the health of the tissue. Two main methods to measure perfusion are based on the Doppler effect and on laser speckle contrast imaging (LSCI). In this chapter we demonstrate a method which augments laser speckle with computational photography for imaging of blood flow speed.

4.1 Theory of LSCI

First, we describe the theoretical background of LSCI. As mentioned in the background chapter (section 2.3), speckle is a statistical phenomenon. We briefly mention here some important properties of speckle [28]:

- The intensity of each speckle grain is a random variable with a decaying expo-

nential distribution:

$$P(I) = \frac{1}{\bar{I}} \exp\left(-\frac{I}{\bar{I}}\right) \quad (4.1)$$

where \bar{I} is the distribution mean which is related to source intensity and imaging geometry.

- The mean (μ) and standard deviation (σ) of a decaying exponential variable are equal. Thus, the contrast $K = \sigma/\mu$ of speckle is unity.
- The size of each speckle grain is given by [84]:

$$S_{speckle} = 2.44\lambda(1 + M)\frac{f}{D} \quad (4.2)$$

where M is the magnification, f is the focal length and D is the aperture size. So larger apertures result in smaller speckle grains. In practice it is common to select the aperture such that the size of a speckle grain is mapped to one pixel.

When the scatteres move, the speckle pattern changes (movement larger than the optical wavelength is sufficient). In the case of bloodflow speed (or any other moving object) there are two time scales of interest:

1. T — the camera exposure time.
2. τ_c — a time scale of the movement (i.e. the time in which the measurement is still correlated to itself).

During the exposure time (T) the camera is integrating over the different speckle patterns (see Fig. 4-1). We note that when the scene is dynamic the speckle pattern (and its contrast) is washed out. In order to model this phenomenon, we start by writing the statistics of each speckle grain (r) [19]:

$$\mu(r) = \frac{1}{T} \int_0^T E \{I(r, t')\} dt' \quad (4.3)$$

$$\sigma^2(r) = \frac{1}{T} \int_0^T 2 \left(1 - \frac{\tau}{T}\right) C^{(2)}(r, \tau) d\tau \quad (4.4)$$

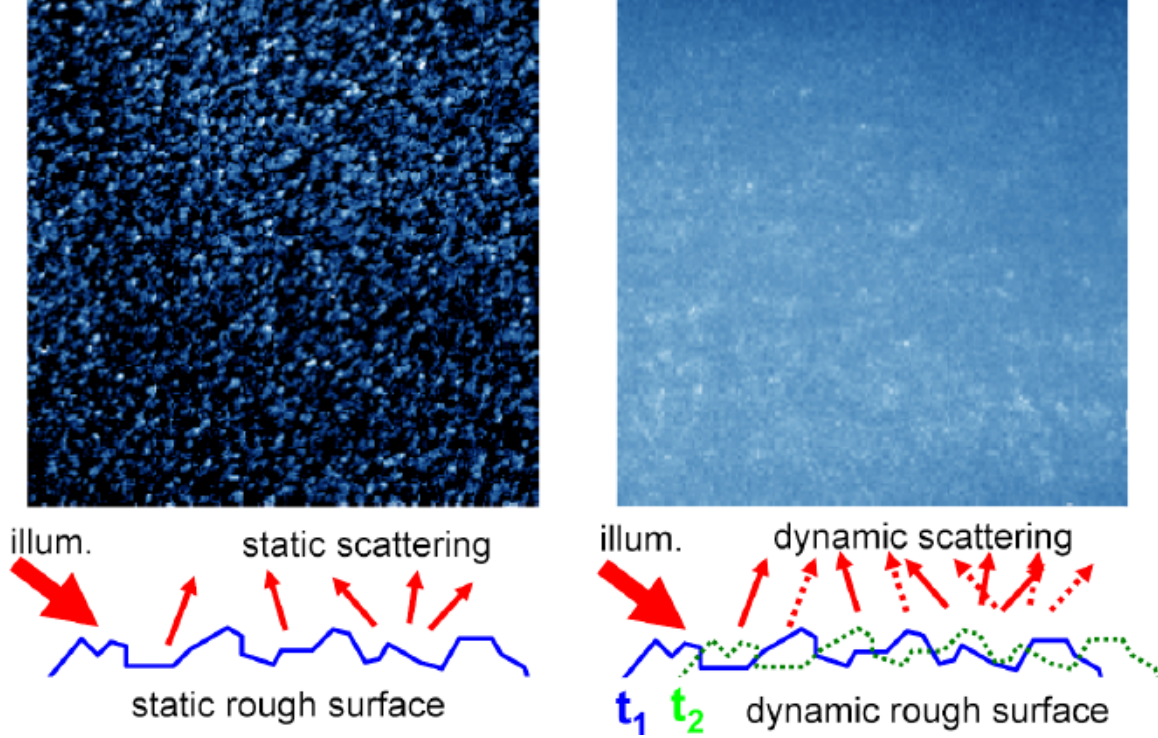


Figure 4-1: Left: speckle formation from a rough static surface has high contrast. Right: Speckle formation from a rough dynamic surface produces low contrast images.

where $E\{\cdot\}$ denotes expectation, $I(r, t')$ is the instantaneous intensity and $C^{(2)}(r, \tau)$ is the covariance of the instantaneous intensity. In order to calculate $C^{(2)}$ it is common to assume [19]: 1) The covariance is a result of a large number of scattering events, thus it can be modeled as a circular Gaussian process and be calculated with the correlation function of the field itself. 2) The movement is a result of Brownian motion, so that the correlation function is a decaying exponential with time scale τ_c . With these assumptions we get:

$$C^{(2)}(r, \tau) = \mu^2(r) \exp\left(-2\frac{|\tau|}{\tau_c}\right) \quad (4.5)$$

We can now calculate the local contrast with Eq. 4.3, 4.4 and 4.5:

$$K(r) = \frac{\sigma(r)}{\mu(r)} = \sqrt{\frac{\tau_c}{2T} \left(2 - \frac{\tau_c}{T} \left(1 - \exp\left(-\frac{2T}{\tau_c}\right)\right)\right)} \quad (4.6)$$

Next, we want to develop a model for the relationship between τ_c and the scatterers' speed V . It is clear that τ_c is inversely proportional to V (faster movement results in shorter correlation time). One common suggestion is [9] :

$$V = \frac{\lambda}{2\pi\tau_c} \quad (4.7)$$

where λ is the optical wavelength. This is a naive, yet common assumption [84]. Making all these assumptions results in a qualitative speed estimation (recent summary of studies on making LSCI a quantitative tool was presented by Briers [7]). Given the qualitative nature of the results, one final approximation can be made. Assuming $T \gg \tau_c$ we get:

$$K(r) = \frac{\sigma(r)}{\mu(r)} \sim \sqrt{\frac{\tau_c}{T}} \quad (4.8)$$

combining Eq. 4.7 and 4.8 we get:

$$V(r) \sim \frac{1}{TK(r)^2} = \frac{1}{T} \left(\frac{\mu(r)}{\sigma(r)} \right)^2 \quad (4.9)$$

Intuitively, we can think of the scatterers movement at a given position as a random process, and Eq. 4.9 suggests we can calculate their speed by measuring the first and second moments of this random process. Three different methods to measure these moments have been suggested:

1. Spatial approximation [9]: for each pixel at position (i, j) we use a neighborhood of $N \times M$ pixels to calculate the statistics. This is essentially assuming the process is ergodic in space. Common neighborhood sizes range from 5×5 to 15×15 . The main disadvantage of this method is the reduction in spatial resolution of the final speed reconstruction.
2. Temporal approximation [14]: in this method a movie is taken, and statistics of each pixel are calculated over time. This is essentially assuming ergodicity in time. The advantage of this method is improved spatial resolution, but it requires a high speed imaging system (in order to account for the ergodicity).

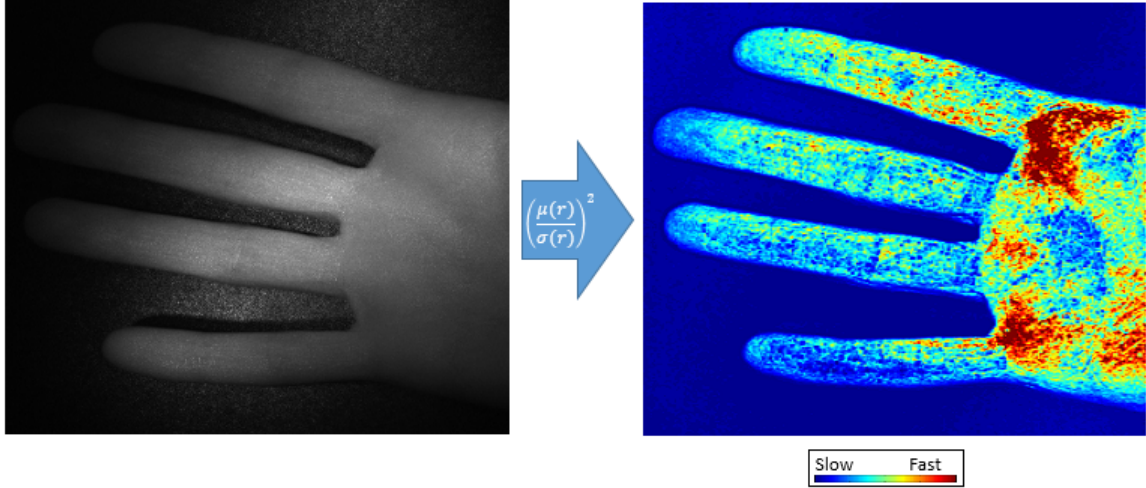


Figure 4-2: An example of mapping from speckle image to perfusion map using Eq. 4.9 and a spatial window.

3. Spatiotemporal approximation [78]: this method combines the two previous methods and uses a neighborhood of $N \times M \times K$ window.

Fig. 4-2 shows an example of a perfusion map of a healthy hand using a spatial window.

4.2 Rejecting Subsurface Scattering for LSCI

It is common to distinguish between light that is directly reflected from a scene to the camera (direct component) and light that scatters within the scene before being reflected to the camera (global component) [66]. In case of skin imaging, each pixel measures contribution from direct reflection and subsurface scattering, see Fig. 4-3. To understand this effect on LSCI we consider the simplified schematic in Fig. 4-4. For a single skin layer, LSCI is straightforward; however, underlying tissue (modeled in Fig. 4-4 [right] as a second scattering layer) makes an unwanted speckle contribution to the contrast image. A known method to separate between the global and direct components of light is known as global-direct separation [66].

When performing global-direct separation, the scene is illuminated with multiple high-frequency patterns. Thus, a set of intensity values are associated with each pixel

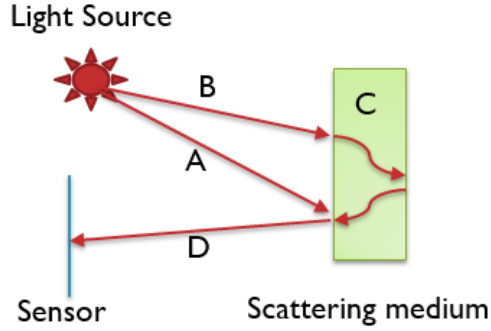


Figure 4-3: Light rays are captured from both the surface and subsurface. The sensor measures the intensity of (D), which is a result of direct illumination (A) and global scattering (B) + (C). Many ray paths can contribute to global light.

(i, j) . The maximum value (L^+) and the minimum value (L^-) can be used to separate direct (D) and global (G) components as [66]:

$$D = \frac{L^+ - L^-}{1 - b} \quad (4.10)$$

$$G = 2 \frac{L^- - bL^+}{1 - b^2} \quad (4.11)$$

Here, b accounts for background illumination.

4.3 Synthetic Results

4.3.1 Simulation Methods

We first evaluate the use of global-direct separation for LSCI with synthetic data. Because rendering dynamic volumetric scattering is challenging, we model a two-layer system. The front layer represents the skin, and the rear layer contains all the scattering of the underlying tissue.

To model coherent scattering (speckle), we proceed as follows: first, the front layer is illuminated with a high-frequency speckle pattern, independent of the sample under study. This pattern strikes the first layer, and scattering is modeled by generating a random intensity pattern with negative exponential statistics. The resulting

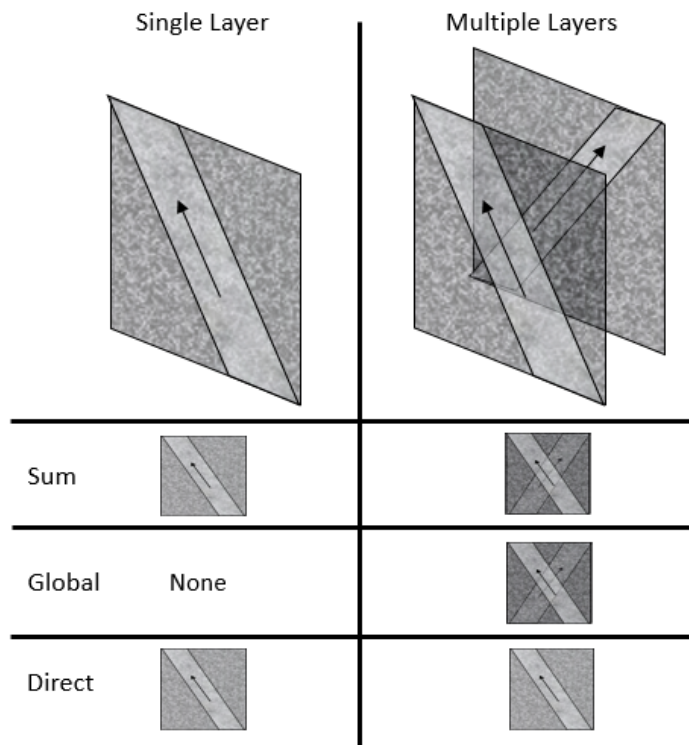


Figure 4-4: Global light produces erroneous contrast maps for skin perfusion. Left: a single layer of dynamic scattering can be reconstructed easily. Right: a second layer compounds the contrast image, and the resulting speed map is incorrect.

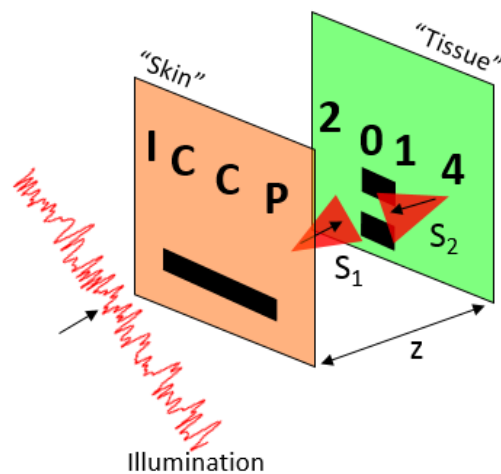


Figure 4-5: Simulated scene with two scattering layers. The black characters indicate areas of high speed. Incident speckle illumination scatters to the first layer, then to the second. Both are recorded simultaneously for four different incident illumination patterns.

speckle pattern is the direct component. Next, a portion of this pattern is transmitted and scattered towards the rear layer. Propagation is accounted for by blurring each speckle. The rear layer forms a second speckle pattern (global component), which is reflected and added to the direct component.

Dynamic speckle is modeled by averaging S realizations of speckle at a pixel, where S is proportional to the velocity at that pixel [28] and the exposure time: $S = VT \sim T/\tau_c$. Thus, higher speeds and longer exposure times imply a larger average, which implies a reduced contrast. The simulation is repeated with N independent speckle illumination patterns, and global-direct decomposition is carried out with the N resulting images.

The blur kernel size is chosen to approximate diffraction. In the paraxial approximation, a speckle of size w_0 blurs to $w(z)$ after a distance z , according to:

$$z = \frac{\pi w_0^2}{\lambda} \sqrt{\left(\frac{w(z)}{w_0}\right)^2 - 1} \quad (4.12)$$

For example, for an average speckle size of 5 pixels, a blur kernel of 20 pixels, a wavelength of $0.750 \mu m$, and a camera pixel size of $5 \mu m$ with unity magnification, Eq. 4.12 implies that the inter-layer distance is $1cm$, which is a typical quantity in biological imaging.

We note here that the high-frequency illumination pattern is itself a random speckle field. This intuitively "matches" the system dynamics and allows us to ignore diffraction from, e.g., the edges of the more conventional checkerboard pattern. The goal of this method is to calculate a relative speed map of the front layer based on $N = 4$ illumination patterns by removing any corruption from the presence of the rear layer.

4.3.2 Simulation Results

The synthetic scene is shown schematically in Fig.4-5, and results are shown in Fig.4-6. Fig.4-6a shows the ground truth speed maps of each layer and a synthetic measurement of each layer in the absence of the other. Note the reduced contrast within the

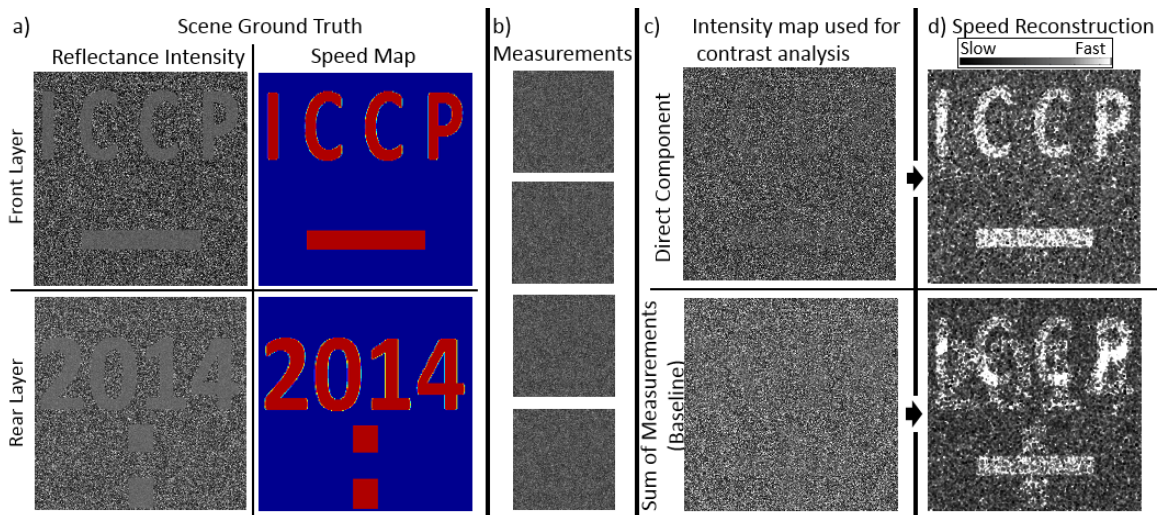


Figure 4-6: Synthetic results demonstrating benefits of global-direct separation for skin perfusion. (a) Scene ground truth: speed maps indicate areas of relative motion, and reflectance maps indicate the contrast measurement of each layer in the absence of the other. (b) Four measurements, illuminated by different speckle patterns. (c) Decomposition to direct component reflectance (top), the sum of measurements as a baseline (bottom). (d) Speed reconstruction based on the corresponding intensity maps. The reconstruction based on the direct component reproduces the speed map of the front layer, whereas the baseline result contains speed contributions from both layers.

characters, where the speed is high. Individual measurements for four illumination patterns are shown in Fig. 4-6b. Though they appear similar, each one is a result of a different speckle illumination pattern. Inputting these measurements into Eq. 4.10, we obtain a direct light image. We reconstruct the speed map based on the contrast of this image (Fig. 4-6c,d [top]). For comparison (Fig. 4-6c,d [bottom]), we see that the standard LSCI reconstructs a speed map that contains information from both layers ("ICCP" and "2014"), whereas the global-direct separation successfully decouples them.

To quantify the simulation results, we normalize all speed maps to the total energy of the ground truth speed map. We define total image energy as the total kinetic energy of the individual pixels:

$$E = \sum_{i,j=1}^n V_{ij}^2 \quad (4.13)$$

where V_{ij} is the speed at pixel (i, j) , and the image is $n \times n$ pixels. The error metric is

$$e_k = \frac{1}{n^2} \sum_{i,j=1}^n \|V_{ij}^{(g)} - V_{ij}^{(k)}\|^2 \quad (4.14)$$

where $V^{(k)}$ is the reconstructed speed map (direct or baseline), and $V^{(g)}$ is the front layer ground truth speed map.

Fig. 4-7 shows the reconstruction error as a function of SNR for different numbers of illumination patterns. We see that both the standard LSCI method (left) and our suggested method (right) improve for increasing N . For $N > 4$, there is no appreciable improvement. With high SNR, our reconstructions produce 50% less error than the baseline LSCI method. Because the direct component is a difference of images (Eq. 4.10), it is susceptible to noise. Therefore, for low SNR, the two methods are comparable. Interestingly, there is a regime of standard LSCI where increasing SNR increases the reconstruction error (dashed line). We expect that this is caused by a small amount of noise, which reduces local contrast and changes the effective local speed.

Fig. 4-8 shows analysis of the reconstruction error for varying distances between

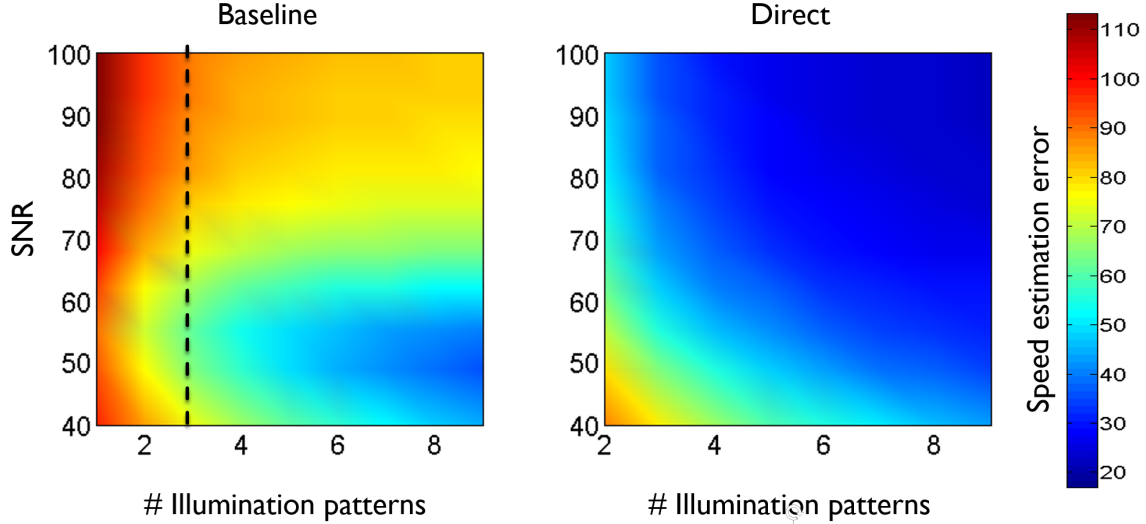


Figure 4-7: Simulation speed reconstruction error for a varying number of illumination sources and measurement noise. The baseline (left) and our suggested method (right) show the reconstruction error for various measurement noise (SNR) and illumination patterns.

layers (a larger distance between layers results in more blurring according to Eq. 4.12). As the distance between the layers increases, the reflected speckle field becomes increasingly blurred, which improves the global-direct separation. On the other hand, the reflections corrupt a wider area of the image and increase the baseline reconstruction error. As N increases, the error is reduced and similarly, above $N > 4$, there is little change.

4.4 Experimental Results

4.4.1 Experimental Prototype

We implement the method in hardware using a Lumenera monochrome camera without an IR filter to image objects approximately 40cm away with a 50mm Nikon lens ($f/2.8$). To implement four illumination patterns, we use four light sources: four 3mW lasers of center wavelength 785nm , placed around the camera lens. To create illumination speckle patterns, each laser passes through a diffusive material (duct tape). The lasers are controlled by an Arduino microcontroller, which is synchro-

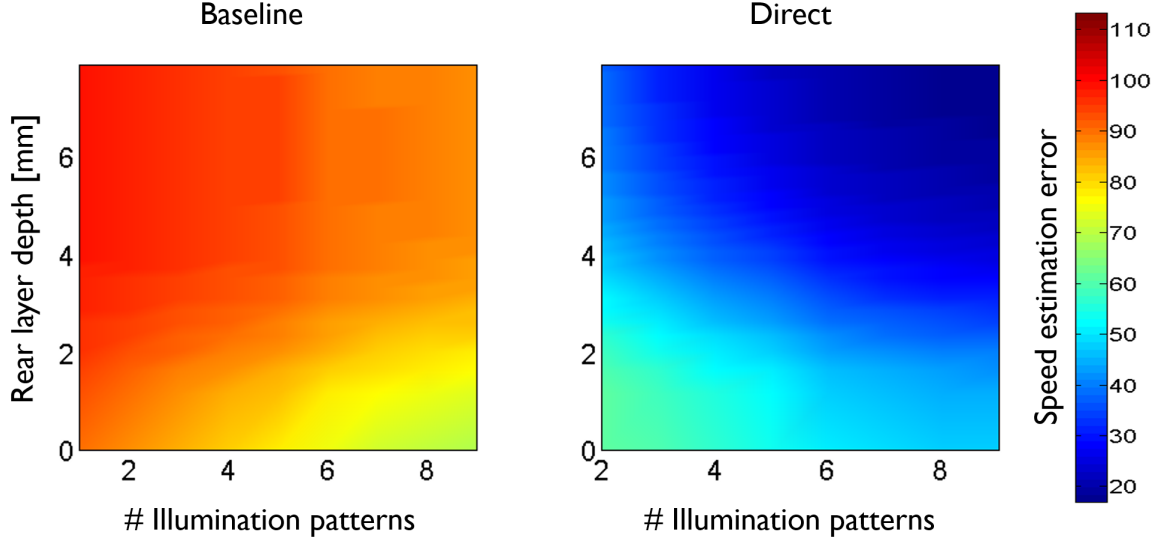


Figure 4-8: Simulation speed reconstruction error for a varying number of illumination sources and internal layer depth z . The baseline (left) and our suggested method (right) show the reconstruction error for various measurement noise (SNR) and illumination patterns.

nized in real time using a Matlab interface (Fig. 4-9). The lasers illuminate the scene sequentially, and the camera records an image for each one with an exposure time of $50ms$. The total acquisition time is approximately one second. The four recorded images are then used to separate global and direct components. Contrast analysis is performed on the direct component, and the speed map is reconstructed. To calculate contrast, we use a spatial window of $N = M = 13$, and the background illumination is $b = 0.01$.

4.4.2 Experimental Results

Fig. 4-10 shows results for a healthy hand. In Fig. 4-10a, the four measurements are shown. Fig. 4-10b is a contrast calculation from the sum of the four measurements (the sum is used to create a uniform illumination over the full field and serves as a baseline). Fig. 4-10c shows the global component image extracted using Eq. 4.11 and the corresponding speed map generated using Eq. 4.9. However, both produce similar erroneous results. Skin perfusion in a normal hand should be uniform, whereas these results have a highly uneven distribution. Finally, Fig. 4-10d shows the direct com-

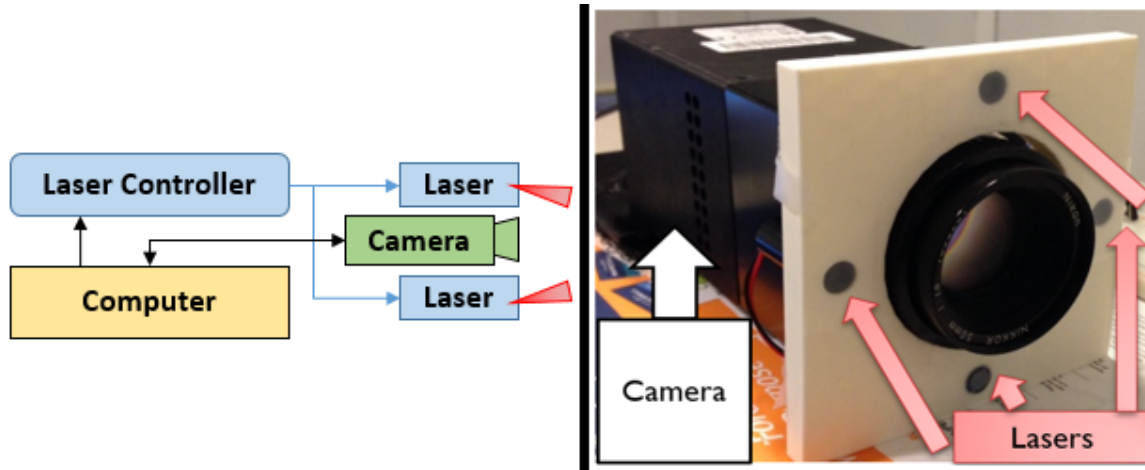


Figure 4-9: Experimental setup. Left: system block diagram. Right: picture of the imaging system used.

ponent image extracted using Eq. 4.10 and the corresponding speed map generated using Eq. 4.9, which demonstrates a much more uniform perfusion map.

Our improvement results from the global component (Fig. 4-10c) being removed so that it no longer corrupts the skin perfusion measurement. Note that the global component contains no speckle while the direct component does contain speckle, and the conventional measurement contains an intermediate amount. Further inspection of the direct speed map reveals two outliers: the tip of the second finger from the top, and the bottom right part of the palm. These areas appear to have low speed associated with them. This can be explained by examining the direct intensity map. We notice these areas appear dark, which means they were not directly illuminated during acquisition. Another notable result is the similarity of the global component to the baseline (both image and speed map) which tells us that the baseline is governed by the global component.

We also show results for a finger with a superficial burn on an otherwise healthy finger (Fig. 4-11). We expect to see low perfusion on the area of the burn, as it is a few days old. Similar qualitative conclusions can be derived here. Of particular interest is the perfusion contrast between the healthy and burn areas of the finger in the direct component measurement, as well as the uniform perfusion on the healthy part of the finger.

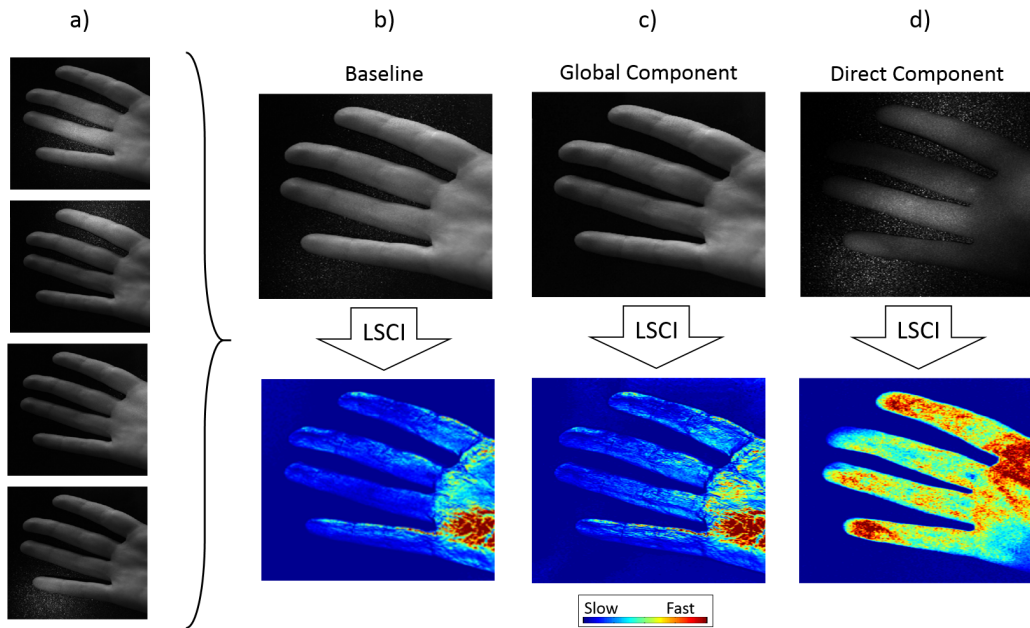


Figure 4-10: Experimental results of a healthy hand. a) The four measurements. Speckle images and corresponding speed maps for baseline (b), global component (c), and direct component (d).

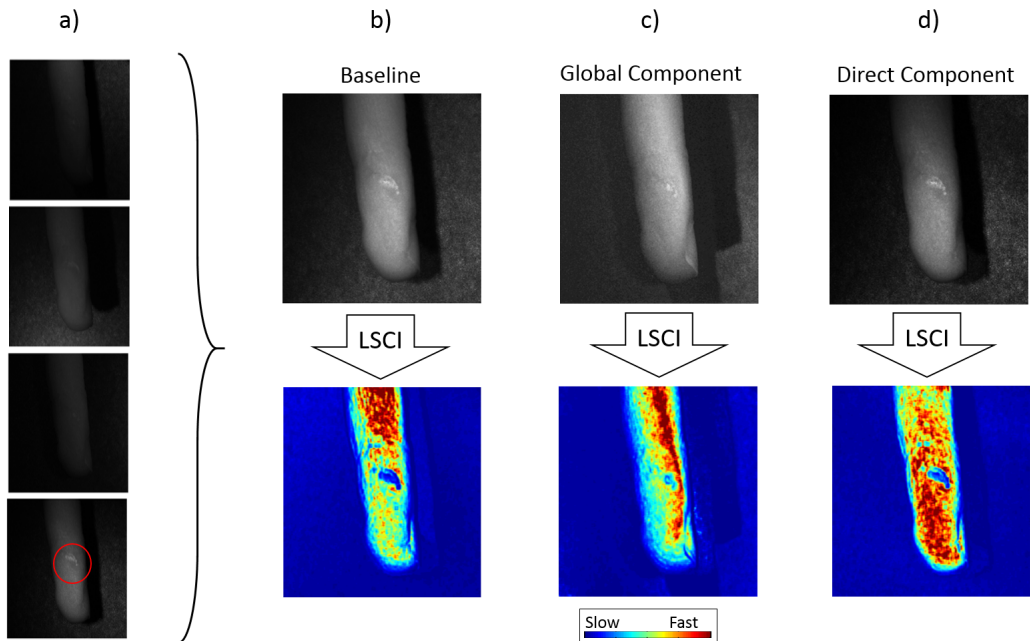


Figure 4-11: Experimental results of a superficial burn. a) the four measurements, the burn is circled in red on the bottom picture. Speckle images and corresponding speed maps for baseline (b), global component (c), and direct component (d).

4.5 Technical Discussion

Our results here indicate that global-direct separation methods, derived from ray optics, have potential use for coherent imaging. This can represent a significant advancement for LSCI and can improve reconstructions of blood flow. Since the suggested method simply adds a new layer in the LSCI pipeline, it can be augmented with any modification and improvement to the basic LSCI algorithm used here.

Applying global-direct separation with coherent illumination is not limited to perfusion and can improve other skin-related analyses, such as extracting biological quantities [91] and improving rendering [42]. It can also improve skin lesion analysis and diagnosis [16].

Our contribution offers a bridge between computational photography and biomedical imaging with intuitive modeling of light scattering. Future efforts in computational photography can be applied towards medical imaging of, e.g., wound healing, burn recovery and skin surgeries.

4.6 Applications and Business Perspective

Perfusion is a fundamental process in tissue, thus skin perfusion measurement can provide information for skin conditions diagnosis. Various skin conditions are highly correlated to socio-economical index, and as such they are more frequent in developing countries. For example, in some parts of India, over 40% of the population suffer from dermatological conditions [29]. Up to 79% of deaths due to skin cancer [41] are caused by Melanoma, which is hard to detect. Some skin conditions may be a result of lifestyle and nutrition; one side effect of Diabetes are diabetic ulcers, which are essentially a case of reduced blood flow to the body extremities, to the point where it may result in an amputation. In India, Diabetes accounts for approximately 80% of all non-traumatic amputations performed every year [32, 2].

The main applications of skin perfusion photography include: wounds and burns diagnosis, cosmetics applications, monitoring of amputations, and assistive technology

in reconstructive and plastic surgeries.

We now discuss the business perspective of this technology and how it might be deployed in India:

- **Key Partners**

Since the technology is meant to target the medical market, the key partners are entities which can support both the development and scaling stages:

- Hospitals — hospitals provide infrastructure and access over time to patients with specific conditions. Without proper support from hospitals for the development and validation stage, there cannot be any scaling.
- Physicians and nurses — the main stakeholders of the technology. They can provide feedback to the value of the technology during the development stage, as well as feedback to the accuracy of the results.
- Universities — local students can assist in rapid-prototyping and quick iterations during the final prototyping stages of the device.
- The health industry — a partner during the scaling stage. The logistic and legal infrastructure of the local industry can be of great value to scale the device quickly.
- NGOs — can help scaling the device beyond big hospitals to local clinics.

- **Key Resources**

The main resource is the intellectual property and the technology developed. The knowledge provides us with better understanding of the physics involved with sub-dermal imaging, which enables better technologies.

Next, a network of physicians and experts both in Cambridge and in India (mostly in Mumbai) provides us with quick and reliable feedback to the results our devices provide, as well as future directions and new conditions to diagnose and monitor.

Lastly, resources that are in constant need are prototyping materials, such as cameras, lasers, and computers.

- **Value Proposition**

The main contribution we can provide is better diagnosis and monitoring for skin-related conditions. Initially, it would be utilized mostly by doctors and nurses. Once the technology becomes reliable, it would scale to personal health-care and enable people better control over their own health. It can democratize healthcare for skin-related conditions, since nowadays patients rely on the expertise of physicians who do not necessarily have good metrics for diagnosis (this is especially true for skin diagnosis). Providing new ways to assess skin conditions will allow patients better understanding of their condition, and possibly enable self-diagnosis.

- **Customer Relationships**

Our main goal is to establish long-term relationships with physicians and patients. Skin conditions, such as significant burns or diabetic ulcers, could be tracked and monitored over time using the device.

- **Channels**

Our main route to deploy the technology is through hospitals, pharmacies and local nurses. Initially, the main users will be physicians in hospitals, where it is easier to initiate a supply chain. At a later stage, when the technology scales to public users, it will be purchased at pharmacies.

- **Customer Segments**

The most important initial customers are hospitals, as they provide infrastructure and access to both patients and physicians. Later, the customer segment will focus on physicians adapting our technology. Finally, when the technology scales, the main segment will be individuals, and the main way to reach them would be through physicians, pharmacies, and private doctors.

- **Cost Structure**

Currently the main costs are development-related, such as prototyping tools.

In the future, costs will shift to clinical trials, and when the device is finalized, to components and manufacturing.

- **Revenue Streams**

One optional revenue would come from selling the device and associated software. Another option is various charging models for the software, for example: one-time payment, payment per diagnosis, and payment per software update.

Chapter 5

Conclusions

In this thesis we develop novel methods to overcome scattering and to use it to our advantage. This is demonstrated in two different cases of scattering. In particular, we show that scattering can encode information on scene parameters, such as movement, as well as allow novel field-of-view formulations and non-traditional, beyond line of sight imaging.

First, we describe a technique to localize and classify fluorescent tags hidden behind turbid layers. This technique uses time-resolved measurements and a novel signal processing framework based on sparse optimization. It shows that although scattering prohibits direct imaging, time-resolved techniques are able to resolve scene geometry even in cases of significant time blur such as fluorescence. Further more, in this case the fluorescence time-blur is used to classify the fluorescence lifetime, which has many biomedical applications. Interestingly, it is shown that more scattering increases the field-of-view of this system, which opens the door to future indirect imaging modalities.

We also use dynamic coherent scattering, which allows assessment of flow speed and skin perfusion. Our method uses a computational photography technique to reject sub-surface scattering in order to improve the speed estimation. We discuss the business perspective and deployment possibilities of this technique in India, for analysis of wounds and burns, and other skin conditions.

Bibliography

- [1] Supreeth Achar, Stephen T Nuske, and Srinivasa G Narasimhan. Compensating for motion during direct-global separation. In *Proceedings of the IEEE International Conference on Computer Vision*, pages 1481–1488, 2013.
- [2] Kleopatra Alexiadou and John Doupis. Management of diabetic foot ulcers. *Diabetes therapy : research, treatment and education of diabetes and related disorders*, 3(1):4, 2012.
- [3] A Aliverdiev. Speckle velocimeter for a self-powered vehicle. *Technical physics*, 47(8), 2002.
- [4] Jacopo Bertolotti, Elbert G van Putten, Christian Blum, Ad Lagendijk, Willem L Vos, and Allard P Mosk. Non-invasive imaging through opaque scattering layers. *Nature*, 491(7423):232–4, November 2012.
- [5] Eric Betzig, George H Patterson, Rachid Sougrat, O Wolf Lindwasser, Scott Olenych, Juan S Bonifacino, Michael W Davidson, Jennifer Lippincott-Schwartz, and Harald F Hess. Imaging intracellular fluorescent proteins at nanometer resolution. *Science (New York, N.Y.)*, 313(5793):1642–1645, September 2006.
- [6] D.A. Boas, D.H. Brooks, E.L. Miller, C.A. DiMarzio, Misha Kilmer, and R.J. Gaudette. Imaging the body with diffuse optical tomography. *IEEE Signal Processing Magazine*, 18(6):57–75, 2001.
- [7] David J Briers, Donald D Duncan, Evan Hirst, Sean J Kirkpatrick, Marcus Larsson, Wiendelt Steenbergen, Tomas Stromberg, and Oliver B Thompson. Laser speckle contrast imaging: theoretical and practical limitations. *Journal of biomedical optics*, 18(6):066018, June 2013.
- [8] J. David Briers. Laser Doppler and time-varying speckle: a reconciliation. *Journal of the Optical Society of America A*, 13(2):345, February 1996.
- [9] J David Briers and Sian Webster. Laser speckle contrast analysis (LASCA): a non-scanning, full-field technique for monitoring capillary blood flow. *Journal of biomedical optics*, 1(2):174–9, April 1996.

- [10] L Brunel, A Brun, P Snabre, and L Cipelletti. Adaptive Speckle Imaging Interferometry: a new technique for the analysis of microstructure dynamics, drying processes and coating formation. *Optics Express*, 15(23):15250, 2007.
- [11] A Cessou, U Meier, and D Stepowski. Applications of planar laser induced fluorescence in turbulent reacting flows. *Measurement Science and Technology*, 11(7):887–901, July 2000.
- [12] Ou Chen, Jing Zhao, Vikash P Chauhan, Jian Cui, Cliff Wong, Daniel K Harris, He Wei, Hee-Sun Han, Dai Fukumura, Rakesh K Jain, and Mounsi G Bawendi. Compact high-quality CdSe-CdS core-shell nanocrystals with narrow emission linewidths and suppressed blinking. *Nature materials*, 12(5):445–451, May 2013.
- [13] Haiying Cheng, Qingming Luo, Qian Liu, Qiang Lu, Hui Gong, and Shaoqun Zeng. Laser speckle imaging of blood flow in microcirculation. *Physics in Medicine and Biology*, 49(7):1347–1357, April 2004.
- [14] Haiying Cheng, Qingming Luo, Shaoqun Zeng, Shangbin Chen, Jian Cen, and Hui Gong. Modified laser speckle imaging method with improved spatial resolution. *Journal of biomedical optics*, 8(3):559–64, July 2003.
- [15] RB Cheng, S and Zimmermann, M and Miles. Separation of time-averaged turbulence components by laser-induced fluorescence. *Physics of Fluids*, 26(4):874–877, April 1983.
- [16] Symon Cotton, Ela Claridge, and Per Hall. A skin imaging method based on a colour formation model and its application to the diagnosis of pigmented skin lesions. *Proceedings of Medical Image . . .*, (d):49–52, 1999.
- [17] B B Das, Feng Liu, and R R Alfano. Time-resolved fluorescence and photon migration studies in biomedical and model random media. *Reports on Progress in Physics*, 60:227–292, 1999.
- [18] A. Davis, S. W. Hasinoff, F. Durand, and W. T. Freeman. Laser speckle photography for surface tampering detection. In *2012 IEEE Conference on Computer Vision and Pattern Recognition*, volume 1, pages 33–40. IEEE, June 2012.
- [19] Donald D Duncan and Sean J Kirkpatrick. Can laser speckle flowmetry be made a quantitative tool? *Journal of the Optical Society of America A*, 25(8):2088, July 2008.
- [20] T. Durduran, A. G. Yodh, B. Chance, and D. A. Boas. Does the photon-diffusion coefficient depend on absorption? *Journal of the Optical Society of America A*, 14(12):3358, December 1997.
- [21] D. J. Durian. The diffusion coefficient depends on absorption. *Optics Letters*, 23(19):1502, October 1998.

- [22] Shechao Feng, Charles Kane, Patrick A Lee, and A Douglas Stone. Correlations and fluctuations of coherent wave transmission through disordered media. *Physical Review Letters*, 61(7):834–837, 1988.
- [23] F. Adolf Fercher and J. David Briers. Flow visualization by means of single-exposure speckle photography. *Optics Communications*, 37(5):326–330, June 1981.
- [24] Ingemar Fredriksson, Marcus Larsson, and Tomas Strömberg. Model-based quantitative laser Doppler flowmetry in skin. *Journal of biomedical optics*, 15(5):057002, 2010.
- [25] Genevieve Gariepy, Nikola Krstajić, Robert Henderson, Chunyong Li, Robert R. Thomson, Gerald S. Buller, Barmak Heshmat, Ramesh Raskar, Jonathan Leach, and Daniele Faccio. Single-photon sensitive light-in-flight imaging. *Nature Communications*, 6:6021, January 2015.
- [26] a P Gibson, J C Hebden, and S R Arridge. Recent advances in diffuse optical imaging. *Physics in Medicine and Biology*, 50(4):R1–R43, February 2005.
- [27] J. W. Goodman, W. H. Huntley, D. W. Jackson, and M. Lehmann. Wavefront-reconstruction imaging through random media. *Applied Physics Letters*, 8(12):311–313, November 1966.
- [28] Joseph W. Goodman. *Speckle Phenomena in Optics: Theory and Applications*. Englewood, Colo. : Roberts & Co., c2007., 2007.
- [29] Nathan Grills, Claire Grills, Tim Spelman, Mark Stooze, Margaret Hellard, Carol El-Hayek, and Rajesh Singh. Prevalence survey of dermatological conditions in mountainous north India. *International Journal of Dermatology*, 51(5):579–587, 2012.
- [30] Mohit Gupta, Amit Agrawal, Ashok Veeraraghavan, and Srinivasa G. Narasimhan. Structured light 3D scanning in the presence of global illumination. In *CVPR 2011*, pages 713–720. IEEE, June 2011.
- [31] Otkrist Gupta, Thomas Willwacher, Andreas Velten, Ashok Veeraraghavan, and Ramesh Raskar. Reconstruction of hidden 3D shapes using diffuse reflections. *Optics express*, 20(17):19096–108, August 2012.
- [32] Sunil Gupta. Management of Diabetic Foot. *Medicine Update*, pages 287–293, 2012.
- [33] Felix Heide, Wolfgang Heidrich, and Matthias B Hullin. Diffuse Mirrors : 3D Reconstruction from Diffuse Indirect Illumination Using Inexpensive Time-of-Flight Sensors. 2014.

- [34] Felix Heide, Lei Xiao, Andreas Kolb, Matthias B Hullin, and Wolfgang Heidrich. Imaging in scattering media using correlation image sensors and sparse convolutional coding. *Optics express*, 22(21):26338–50, October 2014.
- [35] Barmak Heshmat, Guy Satat, Christopher Barsi, and Ramesh Raskar. Single-shot ultrafast imaging using parallax-free alignment with a tilted lenslet array. *Cleo: 2014*, 1(1):STu3E.7, 2014.
- [36] Samuel T Hess, Thanu P K Girirajan, and Michael D Mason. Ultra-high resolution imaging by fluorescence photoactivation localization microscopy. *Biophysical journal*, 91(11):4258–72, December 2006.
- [37] F E Hoge and R N Swift. Airborne simultaneous spectroscopic detection of laser-induced water Raman backscatter and fluorescence from chlorophyll a and other naturally occurring pigments. *Applied optics*, 20(18):3197–3205, September 1981.
- [38] Steven S Hou, William L Rice, Brian J Bacsikai, and Anand T N Kumar. Tomographic lifetime imaging using combined early- and late-arriving photons. *Optics letters*, 39(5):1165–1167, March 2014.
- [39] Bo Huang, Mark Bates, and Xiaowei Zhuang. Super-resolution fluorescence microscopy. *Annual review of biochemistry*, 78:993–1016, January 2009.
- [40] D Huang, E. Swanson, C. Lin, J. Schuman, W. Stinson, W Chang, M. Hee, T Flotte, K Gregory, C. Puliafito, and Al. Et. Optical coherence tomography. *Science*, 254(5035):1178–1181, November 1991.
- [41] A F Jerant, J T Johnson, C D Sheridan, and T J Caffrey. Early detection and treatment of skin cancer. *American family physician*, 62(2):357–368, 375–376, 381–382, 2000.
- [42] Jorge Jimenez, Tim Weyrich, Timothy Scully, Nuno Barbosa, Craig Donner, Xenxo Alvarez, Teresa Vieira, Paul Matts, Verónica Orvalho, and Diego Gutierrez. A practical appearance model for dynamic facial color. *ACM SIGGRAPH Asia 2010 papers on - SIGGRAPH ASIA '10*, 29(6):1, 2010.
- [43] Chenfei Jin, Zitong Song, Siqi Zhang, Jianhua Zhai, and Yuan Zhao. Recovering three-dimensional shape through a small hole using three laser scatterings. *Optics letters*, 40(1):52–5, January 2015.
- [44] Achuta Kadambi, Hayato Ikoma, Xing Lin, Gordon Wetzstein, and Ramesh Raskar. Subsurface Enhancement through Sparse Representations of Multi-spectral Direct/Global Decomposition. In *Imaging and Applied Optics*, page CTh1B.4, Washington, D.C., 2013. OSA.
- [45] Achuta Kadambi, Hang Zhao, Boxin Shi, Ramesh Raskar, and Related Work. Occluded Imaging with Time of Flight Sensors. 2013.

- [46] Ori Katz, Pierre Heidmann, Mathias Fink, and Sylvain Gigan. Non-invasive single-shot imaging through scattering layers and around corners via speckle correlations. *Nature Photonics*, 8(10):784–790, August 2014.
- [47] Ori Katz, Eran Small, Yaron Bromberg, and Yaron Silberberg. Focusing and compression of ultrashort pulses through scattering media. *Nature Photonics*, 5(6):372–377, May 2011.
- [48] Ori Katz, Eran Small, Yefeng Guan, and Yaron Silberberg. Noninvasive non-linear focusing and imaging through strongly scattering turbid layers. *Optica*, 1(3):170, September 2014.
- [49] Ori Katz, Eran Small, and Yaron Silberberg. Looking around corners and through thin turbid layers in real time with scattered incoherent light. *Nature Photonics*, 6(8):549–553, July 2012.
- [50] Toshihiro Kobayashi, Mohit Gupta, and Shree K. Nayar. Multiplexed illumination for scene recovery in the presence of global illumination. In *2011 International Conference on Computer Vision*, pages 691–698. IEEE, November 2011.
- [51] H. KOGELNIK and K. S. PENNINGTON. Holographic Imaging Through a Random Medium. *Journal of the Optical Society of America*, 58(2):273, February 1968.
- [52] Anand T N Kumar. Tomographic fluorescence lifetime imaging. In Laura Marcu, Paul French, and Daniel Elson, editors, *Fluorescence Lifetime Spectroscopy and Imaging*, pages 461–476. CRC Press, July 2014.
- [53] M Le Thinh, Joseph S Paul, H Al-Nashash, A Tan, a R Luft, F S Sheu, and S H Ong. New insights into image processing of cortical blood flow monitors using laser speckle imaging. *IEEE transactions on medical imaging*, 26(6):833–42, June 2007.
- [54] EMMETT N. LEITH and JURIS UPATNIEKS. Holographic Imagery Through Diffusing Media. *Journal of the Optical Society of America*, 56(4):523, April 1966.
- [55] Pengcheng Li, Songlin Ni, Li Zhang, Shaoqun Zeng, and Qingming Luo. Imaging cerebral blood flow through the intact rat skull with temporal laser speckle imaging. *Optics Letters*, 31(12):1824, 2006.
- [56] Jeff W Lichtman and José-Angel Conchello. Fluorescence microscopy. *Nature methods*, 2(12):910–919, December 2005.
- [57] Xinhao Liu, Masayuki Tanaka, and Masatoshi Okutomi. Single-image noise level estimation for blind denoising. *IEEE transactions on image processing : a publication of the IEEE Signal Processing Society*, 22(12):5226–37, December 2013.

- [58] T. Loupas, W.N. McDicken, and P.L. Allan. An adaptive weighted median filter for speckle suppression in medical ultrasonic images. *IEEE Transactions on Circuits and Systems*, 36(1):129–135, January 1989.
- [59] G D Mahan, W E Engler, J J Tiemann, and E Uzgiris. Ultrasonic tagging of light : Theory. 95(November):14015–14019, 1998.
- [60] Joshua K Meisner, Suna Sumer, Kelsey P Murrell, Timothy J Higgins, and Richard J Price. Laser speckle flowmetry method for measuring spatial and temporal hemodynamic alterations throughout large microvascular networks. *Microcirculation (New York, N.Y. : 1994)*, 19(7):619–31, October 2012.
- [61] Joseph D. Miller, Mikhail Slipchenko, Terrence R. Meyer, Naibo Jiang, Walter R. Lempert, and James R. Gord. Ultrahigh-frame-rate OH fluorescence imaging in turbulent flames using a burst-mode optical parametric oscillator. *Optics Letters*, 34(9):1309–1311, April 2009.
- [62] Allard P. Mosk, Ad Lagendijk, Geoffroy Lerosey, and Mathias Fink. Controlling waves in space and time for imaging and focusing in complex media. *Nature Photonics*, 6(5):283–292, May 2012.
- [63] Nikhil Naik, Christopher Barsi, Andreas Velten, and Ramesh Raskar. Estimating wide-angle, spatially varying reflectance using time-resolved inversion of backscattered light. *Journal of the Optical Society of America. A, Optics, image science, and vision*, 31(5):957–963, May 2014.
- [64] Nikhil Naik, Shuang Zhao, Andreas Velten, Ramesh Raskar, and Kavita Bala. Single view reflectance capture using multiplexed scattering and time-of-flight imaging. *ACM Transactions on Graphics*, 30(6):1, December 2011.
- [65] S.M. Massachusetts Institute of Technology Naik, Nikhil. Multibounce light transport analysis using ultrafast imaging for material acquisition, 2012.
- [66] Shree K. Nayar, Gurunandan Krishnan, Michael D. Grossberg, and Ramesh Raskar. Fast separation of direct and global components of a scene using high frequency illumination. *ACM Transactions on Graphics*, 25(3):935, July 2006.
- [67] Vasilis Ntziachristos. Going deeper than microscopy: the optical imaging frontier in biology. *Nature methods*, 7(8):603–14, August 2010.
- [68] M. O’Toole, A. Velten, A. Agrawal, and R. Raskar. Decomposing global light transport using time of flight imaging. In *2012 IEEE Conference on Computer Vision and Pattern Recognition*, pages 366–373. IEEE, June 2012.
- [69] Matthew O’Toole, Ramesh Raskar, and Kiriakos N. Kutulakos. Primal-dual coding to probe light transport. *ACM Transactions on Graphics*, 31(4):1–11, July 2012.

- [70] Borlan Pan, Reena Chakraborty, and Kris A. Berglund. Time resolved fluorescence and anisotropy of 1-pyrene butyric acid and pyranine as probes of solvent organization in sucrose solutions. *Journal of Crystal Growth*, 130(3-4):587–599, June 1993.
- [71] Y.C. Pati, R. Rezaiifar, and P.S. Krishnaprasad. Orthogonal matching pursuit: recursive function approximation with applications to wavelet decomposition. In *Proceedings of 27th Asilomar Conference on Signals, Systems and Computers*, pages 40–44. IEEE Comput. Soc. Press, 1993.
- [72] Perimed (R). PeriCam PSI System <http://www.perimed-instruments.com/>.
- [73] E. Pino, A.M. Campos, and E. Lissi. Changes in pyranine absorption and emission spectra arising from its complexation to 2,2'-azobis(2-amidinopropane). *Journal of Photochemistry and Photobiology A: Chemistry*, 155(1-3):63–68, February 2003.
- [74] Jia Qin, Roberto Reif, Zhongwei Zhi, Suzan Dziennis, and Ruikang Wang. Hemodynamic and morphological vasculature response to a burn monitored using a combined dual-wavelength laser speckle and optical microangiography imaging system. *Biomedical optics express*, 3(3):455–66, March 2012.
- [75] Roberto A Rabal, Hector J and Braga Jr. *Dynamic laser speckle and applications*. CRC Press, 2010.
- [76] Dan Raviv, Christopher Barsi, Nikhil Naik, Micha Feigin, and Ramesh Raskar. Pose estimation using time-resolved inversion of diffuse light. *Optics Express*, 22(17):20164, August 2014.
- [77] Scott B Raymond, David A Boas, Brian J Bacskai, and Anand T N Kumar. Lifetime-based tomographic multiplexing. *Journal of biomedical optics*, 15(4):046011, January 2010.
- [78] Abhishek Rege, Janaka Senarathna, Nan Li, and Nitish V Thakor. Anisotropic processing of laser speckle images improves spatiotemporal resolution. *IEEE transactions on bio-medical engineering*, 59(5):1272–80, May 2012.
- [79] Michael J Rust, Mark Bates, and Xiaowei Zhuang. Sub-diffraction-limit imaging by stochastic optical reconstruction microscopy (STORM). *Nature methods*, 3(10):793–796, October 2006.
- [80] Guy Satat, Christopher Barsi, and Ramesh Raskar. Skin perfusion photography. In *2014 IEEE International Conference on Computational Photography (ICCP)*, pages 1–8. IEEE, May 2014.
- [81] Guy Satat, Barmak Heshmat, Christopher Barsi, Dan Raviv, Ou Chen, Mouni G Bawendi, and Ramesh Raskar. Locating and classifying fluorescent tags behind turbid layers using time-resolved inversion. *Nature Communications*, 6, 2015.

- [82] J M Schmitt, S H Xiang, and K M Yung. Speckle in optical coherence tomography. *Journal of biomedical optics*, 4(1):95–105, January 1999.
- [83] Pradeep Sen, Billy Chen, Gaurav Garg, Stephen R. Marschner, Mark Horowitz, Marc Levoy, and Hendrik P. A. Lensch. Dual photography. *ACM Transactions on Graphics*, 24(3):745–755, July 2005.
- [84] Janaka Senarathna, Abhishek Rege, Nan Li, and Nitish V Thakor. Laser Speckle Contrast Imaging: theory, instrumentation and applications. *IEEE reviews in biomedical engineering*, 6:99–110, January 2013.
- [85] Alok Kumar Singh, Dinesh N Naik, Giancarlo Pedrini, Mitsuo Takeda, and Wolfgang Osten. Looking through a diffuser and around an opaque surface : A holographic approach. 22(7):7694–7701, 2014.
- [86] Michael S. D. Smith, Ernie F. Packulak, and Michael G. Sowa. Development of a laser speckle imaging system for measuring relative blood flow velocity. volume 6343, pages 634304–634304–8, September 2006.
- [87] C J Stewart, C L Gallant-Behm, K Forrester, J Tulip, D a Hart, and R C Bray. Kinetics of blood flow during healing of excisional full-thickness skin wounds in pigs as monitored by laser speckle perfusion imaging. *Skin research and technology : official journal of International Society for Bioengineering and the Skin (ISBS) [and] International Society for Digital Imaging of Skin (ISDIS) [and] International Society for Skin Imaging (ISSI)*, 12(4):247–53, November 2006.
- [88] Vincent Studer, Jérôme Bobin, Makhlad Chahid, Hamed Shams Mousavi, Emmanuel Candes, and Maxime Dahan. Compressive fluorescence microscopy for biological and hyperspectral imaging. *Proceedings of the National Academy of Sciences of the United States of America*, 109(26):E1679–87, June 2012.
- [89] Oliver Thompson, Jimmy Bakker, Carla Kloeze, Erwin Hondebrink, and Wieldt Steenbergen. Experimental comparison of perfusion imaging systems using multi-exposure laser speckle, single-exposure laser speckle, and full-field laser Doppler. In *Dynamics and Fluctuations in Biomedical Photonics IX*, page 822204, February 2012.
- [90] Abbie E. Tippie and James R. Fienup. Phase-error correction for multiple planes using a sharpness metric. *Optics Letters*, 34(5):701, February 2009.
- [91] Norimichi Tsumura, Nobutoshi Ojima, Kayoko Sato, Mitsuhiro Shiraishi, Hideto Shimizu, Hirohide Nabeshima, Syuuichi Akazaki, Kimihiko Hori, and Yoichi Miyake. Image-based skin color and texture analysis/synthesis by extracting hemoglobin and melanin information in the skin. In *ACM SIGGRAPH 2003 Papers on - SIGGRAPH '03*, page 770, New York, New York, USA, 2003. ACM Press.

- [92] I. M. Vellekoop and A. P. Mosk. Focusing coherent light through opaque strongly scattering media. *Optics Letters*, 32(16):2309, 2007.
- [93] Andreas Velten, Ramesh Raskar, Di Wu, Adrian Jarabo, Belen Masia, Christopher Barsi, Chinmaya Joshi, Everett Lawson, Mounqi Bawendi, and Diego Gutierrez. Femto-photography. *ACM Transactions on Graphics*, 32(4):1, July 2013.
- [94] Andreas Velten, Thomas Willwacher, Otkrist Gupta, Ashok Veeraraghavan, Mounqi G Bawendi, and Ramesh Raskar. Recovering three-dimensional shape around a corner using ultrafast time-of-flight imaging. *Nature communications*, 3:745, January 2012.
- [95] Alfred Vogel and Vasan Venugopalan. Mechanisms of pulsed laser ablation of biological tissues. *Chemical reviews*, 103(2):577–644, February 2003.
- [96] L Wang, P P Ho, C Liu, G Zhang, and R R Alfano. Ballistic 2-d imaging through scattering walls using an ultrafast optical kerr gate. *Science (New York, N.Y.)*, 253(5021):769–71, August 1991.
- [97] Lidai Wang, Jun Xia, Junjie Yao, Konstantin I. Maslov, and Lihong V. Wang. Ultrasonically Encoded Photoacoustic Flowgraphy in Biological Tissue. *Physical Review Letters*, 111(20):204301, November 2013.
- [98] Lihong Wang. Mechanisms of Ultrasonic Modulation of Multiply Scattered Coherent Light: An Analytic Model. *Physical Review Letters*, 87(4):043903, July 2001.
- [99] Lihong V. Wang and Hsin-I Wu. *Biomedical Optics: Principles and Imaging*. John Wiley & Sons, 2012.
- [100] Lihong V Wang and Song Hu. Photoacoustic tomography: in vivo imaging from organelles to organs. *Science (New York, N.Y.)*, 335(6075):1458–62, March 2012.
- [101] George M. Williams, Jr., Thomas Allen, Charles Dupuy, Thomas Novet, and David Schut. Optically coded nanocrystal taggants and optical frequency IDs. In *SPIE Defense, Security, and Sensing*, page 76730M. International Society for Optics and Photonics, April 2010.
- [102] Xiao Xu, Honglin Liu, and Lihong V. Wang. Time-reversed ultrasonically encoded optical focusing into scattering media. *Nature Photonics*, 5(3):154–157, January 2011.
- [103] K. M. Yoo, Feng Liu, and R. R. Alfano. Imaging through a scattering wall using absorption. *Optics Letters*, 16(14):1068, July 1991.

- [104] Pavel Zakharov, Andreas Völker, Alfred Buck, Bruno Weber, and Frank Scheffold. Quantitative modeling of laser speckle imaging. *Optics Letters*, 31(23):3465, June 2006.
- [105] Jan Zizka, Alex Olwal, and Ramesh Raskar. SpeckleSense. In *Proceedings of the 24th annual ACM symposium on User interface software and technology - UIST '11*, page 489, New York, New York, USA, 2011. ACM Press.